JPEDAV (2009) 30:443–461
DOI: 10.1007/s11669-009-9569-z
1547-7037 ©ASM International

Thermodynamic Database for the Al-Ca-Co-Cr-Fe-Mg-Mn-Ni-Si-O-P-S System and Applications in Ferrous Process Metallurgy

Sergei A. Decterov, Youn-Bae Kang, and In-Ho Jung

(Submitted March 31, 2009; in revised form June 19, 2009)

Computerized thermodynamic databases for solid and liquid metals, slag, and solid oxide phases in the Al_2O_3-CaO-CoO-CrO-Cr_2O_3-FeO-Fe_2O_3-MgO-MnO-NiO-SiO_2 system (with dissolved S and P) have been developed by critical evaluation/optimization of various available phase equilibrium and thermodynamic data. The databases contain parameters of models specifically developed for molten slags, liquid steel, and solid oxide solutions such as spinel, pyroxenes, olivine, monoxide (wustite, periclase, lime), corundum, etc. By means of the optimization process, model parameters are found which reproduce various thermodynamic and phase equilibrium data within experimental error limits. Furthermore, the models permit extrapolation into regions of temperature and composition where data are not available. The databases are automatically accessed by user-friendly software that calculates complex equilibria involving slag, metals, refractories, and gases simultaneously, for systems with many components, over wide ranges of temperature, oxygen potential, and pressure. A short review of the available databases is presented. The critical evaluation/optimization procedure is outlined using the Al_2O_3-CaO-FeO-Fe_2O_3-MgO-SiO_2 and Al_2O_3-CaO-MnO-SiO_2 systems as examples. Several applications of the databases to deoxidation, dehydrogenation, and dephosphorization of iron and to inclusion control in steel are discussed.

Keywords databases, ferrous metallurgy, inclusion control, oxide systems, phase diagrams, phase equilibrium, refining, slags, steelmaking, thermodynamics

1. Introduction

In recent years, thermodynamic modeling has been actively pursued apace with the improvement of computational techniques and software. Based on a proper thermodynamic model for every phase of a given system, various available thermodynamic and phase equilibrium data for the system are critically evaluated simultaneously to obtain one self-consistent set of model parameters for the Gibbs energies which best reproduce the data for all phases as functions of temperature and composition. This technique has come to be known as thermodynamic "optimization." Where data are lacking for a multicomponent system, the models and optimized model parameters for lower-order (binary and ternary) subsystems can be used to provide good estimates.

In this way, thermodynamic databases are developed. The databases are then used, along with Gibbs energy minimization software, to calculate multicomponent phase equilibria of importance for various applications. Over the last 4 years, several databases have been developed by the authors with the view to facilitate simulations of industrial processes in iron and steelmaking.

In this article, we shall outline the technique of database development by critical evaluation/optimization. The chemical system that has been critically evaluated for applications in iron and steelmaking will be briefly reviewed to give an idea of the major phases and phase equilibria in such a system. Finally, several examples will be presented to demonstrate the versatility and accuracy of the developed thermodynamic databases to calculations which are important for steel refining and inclusion engineering.

2. Thermodynamic Databases

The selection of proper databases for a given system is a prerequisite for accurate thermodynamic calculations. The

---

This article is an invited paper selected from participants of the 14th National Conference and Multilateral Symposium on Phase Diagrams and Materials Design in honor of Prof. Zhanpeng Jin's 70th birthday, held November 3-5, 2008, in Changsha, China. The conference was organized by the Phase Diagrams Committee of the Chinese Physical Society with Drs. Huashan Liu and Libin Liu as the key organizers. Publication in *Journal of Phase Equilibria and Diffusion* was organized by J.-C. Zhao, The Ohio State University; Yong Du, Central South University; and Qing Chen, Thermo-Calc Software AB.

Sergei A. Decterov and **Youn-Bae Kang**, Dép. de Génie Chimique, Centre de Recherche en Calcul Thermochimique, École Polytechnique de Montréal, P.O. Box 6079 Station "Downtown", Montreal, QC H3C 3A7, Canada; **In-Ho Jung**, Department of Mining and Materials Engineering, McGill University, Montreal, QC H3A 2B2, Canada. Contact e-mail: sergei.decterov@polymtl.ca.

databases must be thermodynamically self-consistent; otherwise very erroneous results can often occur.

The FACT databases[1] for multicomponent oxide, salt, alloy, and aqueous solutions have been developed by critical evaluation/optimization over the last 30 years. The databases contain over 4400 compounds and 120 nonideal multicomponent solution phases. The FACT databases were used for the calculations presented in this article.

The FACT oxide solution database contains critically evaluated thermodynamic data for the molten slag phase and for many extensive solid oxide solutions containing the following components: Al_2O_3, As_2O_3, B_2O_3, CaO, CoO, CrO, Cr_2O_3, Cu_2O, FeO, Fe_2O_3, GeO_2, K_2O, Na_2O, MgO, MnO, NiO, P_2O_5, PbO, SiO_2, SnO, TiO_2, Ti_2O_3, ZnO, and ZrO_2. Not all possible combinations of these components have been critically evaluated. Generally, the critical assessment and optimization of model parameters have been done for certain subsystems of this 24-component system which are of particular importance for various applications in materials science, ceramics, geology, petrochemistry, corrosion, metallurgy (pyro-, hydro-, electro-) combustion, energy, glass technology, etc. As an example, the critical evaluation/optimization procedure for developing the oxide database (on a smaller scale) will be outlined in the next section.

The molten slag phase is modeled by the Modified Quasichemical Model[2-4] in which short-range ordering is taken into account. Ceramic solid solutions are mainly modeled in the framework of the Compound Energy Formalism,[5] taking into account the crystal structure and physical nature of each solution. For example, the model for spinel[6] describes the distribution of cations and vacancies over tetrahedral (T) and octahedral (O) sites: $(Al^{3+}, Co^{2+}, Co^{3+}, Cr^{2+}, Cr^{3+}, Fe^{2+}, Fe^{3+}, Mg^{2+}, Ni^{2+}, Zn^{2+})^T[Al^{3+}, Co^{2+}, Co^{3+}, Cr^{3+}, Fe^{2+}, Fe^{3+}, Mg^{2+}, Ni^{2+}, Zn^{2+}, Va]_2^O O_4$. The olivine solution is modeled by considering two octahedral sites: $[Ca^{2+}, Co^{2+}, Fe^{2+}, Mg^{2+}, Mn^{2+}, Ni^{2+}, Zn^{2+}]^{M2}(Ca^{2+}, Co^{2+}, Fe^{2+}, Mg^{2+}, Mn^{2+}, Ni^{2+}, Zn^{2+})^{M1}SiO_4$. The mixing of cations on three sublattices was taken into account for melilite and pyroxenes. Because the thermodynamic model used for each phase in the FACT database has been chosen with consideration of the actual structure of the phase, the predictive ability is very high for estimating the properties of multicomponent solutions.

The solubilities of S, SO_4, CO_3, H_2O, OH, F, Cl, Br, and I in molten slags were modeled by the Blander-Reddy Capacity Model.[7,8] In this model, dissolved anions such as S^{2-} are assumed to form ideal solutions, substituting for O^{2-} and $SiO_4{}^{4-}$ anions in the oxide-silicate liquid. From this simple assumption, solubilities (capacities) of sulfide, sulfate, etc. can be predicted with good accuracy.[7]

Recently, a new FACT database for liquid steel was developed based on a new model that incorporates the MeO and Me_2O oxide associates[9] to accurately describe deoxidation phenomena in liquid steel. This database has been developed for 15 deoxidation systems Fe-M-O (M = Al, B, Ba, Ca, Ce, Cr, La, Mg, Mn, Nb, Si, Ta, Ti, V, Zr),[9] and has high predictive ability for multicomponent systems. The calculation of deoxidation equilibria in steel will be illustrated in the following sections (Sections 4.3 and 4.4) in more detail. Similar sulfide associates were introduced to allow desulphurization calculations.

The database for liquid steel is now part of a complete FactSage database for steel alloys.[1] It includes the following elements: Al, B, Bi, C, Ca, Ce, Co, Cr, Cu, Fe, La, Mg, Mn, Mo, N, O, Nb, Ni, P, Pb, S, Sb, Si, Sn, Ti, V, W, and Zr. This database is based on relevant steel subsystems from the old (2001) SGTE Solution Database,[10] but now incorporating updates of those systems as well as new published assessments.[11] This database contains assessed data for alloy and carbonitride phases: liquid, fcc, bcc, hcp, cementite, laves phase, carbides, sigma phase, etc. This database is compatible with the FACT oxide database. All solutions in the steel database were modeled using the Compound Energy Formalism.

The Gibbs energy minimization software of the FactSage[1] thermochemical computing system was used to perform the thermodynamic calculations in this work. The FACT databases discussed above are automatically accessed by this user-friendly software. Users can perform complex equilibrium calculations for systems with many components involving slag, steel, inclusions, refractories, and gases simultaneously over wide ranges of temperature, oxygen potential, and pressure.

3. Oxide Database Development for Ferrous Process Metallurgy

Thermodynamic databases are prepared by the following thermodynamic "optimization" procedure:

1. For each particular solution, an appropriate model is developed, which is based upon the physical nature and structure of the solution. The model gives the functional dependence of the thermodynamic properties of the solution on temperature and composition.
2. Then, one set of self-consistent parameters of the models is obtained for all phases in a chemical system of interest. Various available thermodynamic and phase equilibrium data from the literature are critically evaluated and used to select model parameters. Through the use of FactSage calculations, discrepancies in the available data often become evident and can be resolved. For example, if activities of components A and B in a binary solution A-B were measured, they are not independent and must obey the Gibbs-Duhem equation. If a model fits well the activity of A, but not the activity of B, this is an indication that the data for activities of A and B are internally contradictory. FactSage automatically takes into account all thermodynamic laws and interrelations between thermodynamic functions and phase equilibria; therefore, interpolations and extrapolations can be made in a thermodynamically correct manner. When the crucial data are not available or the contradictions between various sets of data cannot be resolved, our experimentalist collaborators are asked to make a few experiments at selected temperatures and compositions

to constrain the models. This is done for all 2-component, 3-component (and, if data are available, higher-order) subsystems of a given chemical system.

3. Next, the solution models with parameters calibrated based on experimental data for lower-order subsystems are used to estimate the thermodynamic properties of multicomponent solutions. If some multicomponent experimental data are available, they are used to verify the predictive ability of the models. Finally, multicomponent phase equilibria are calculated for simulation of industrial processes.

Over the last several years, these techniques have been applied systematically for the evaluation of dozens of oxide systems of importance to iron and steelmaking. In this way, the vast amount of thermodynamic data amassed over the past decades is being critically evaluated and correlated, extended to the prediction of properties of multicomponent solutions, and made readily available to the industrial and academic communities.

The six-component system, Al_2O_3-CaO-FeO-Fe_2O_3-MgO-SiO_2, which is important for most applications of the oxide database, has been completely re-optimized using the new powerful models developed for the liquid slag and multicomponent solid solutions such as spinel, pyroxenes, olivine, melilite, monoxide, etc. Parameters of the models have been optimized to represent many thousands of experimental points. All this experimental information from thousands of publications has been critically evaluated, made self-consistent, and condensed to several dozens model parameters in the oxide database. These models have made it possible to reproduce various experimental data within experimental error limits from 25 °C to above the liquidus temperatures, at all compositions and oxygen partial pressures from saturation with metals to equilibrium with oxygen.

In a single article it is not possible to give even a brief overview of all thermodynamic and phase equilibrium data that have been taken into account. Figures 1 to 5 present a series of calculated liquidus projections for the ternary subsystems of the Al_2O_3-CaO-FeO-Fe_2O_3-MgO-SiO_2 system which are of most importance to ferrous and nonferrous process metallurgy.[12,17-19] The optimized phase diagrams for the Al_2O_3-CaO-SiO_2 system and its binary subsystems and for the Fe-O system have been published elsewhere.[6,20] These figures give an idea of the major phases and phase equilibria in the Al_2O_3-CaO-FeO-Fe_2O_3-MgO-SiO_2 system. Of course, many other types of phase diagrams and other data such as all thermodynamic properties, activities, Fe^{2+}/Fe^{3+} ratios, distributions of cations between different sublattices in solid solutions, partial pressures of equilibrium gaseous species, etc. have also been reproduced during the optimization processes, and can be calculated and plotted by the software.

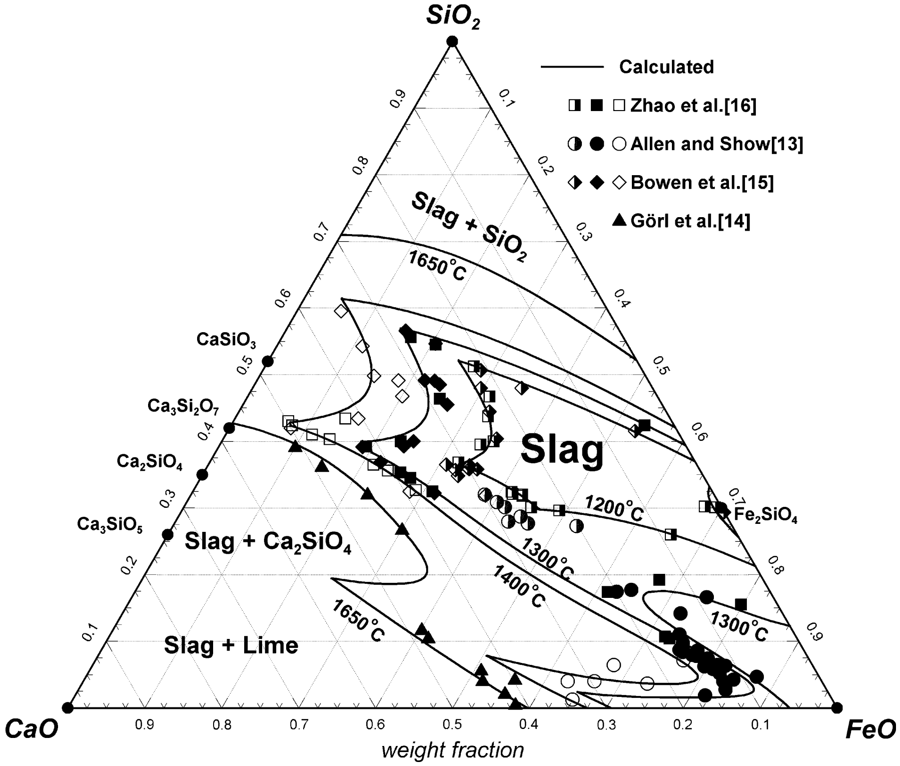

Fig. 1 Calculated liquidus[12] of the Ca-Fe-Si-O system in equilibrium with iron at temperatures between 1200 and 1650 °C compared with experimental data[13-16]

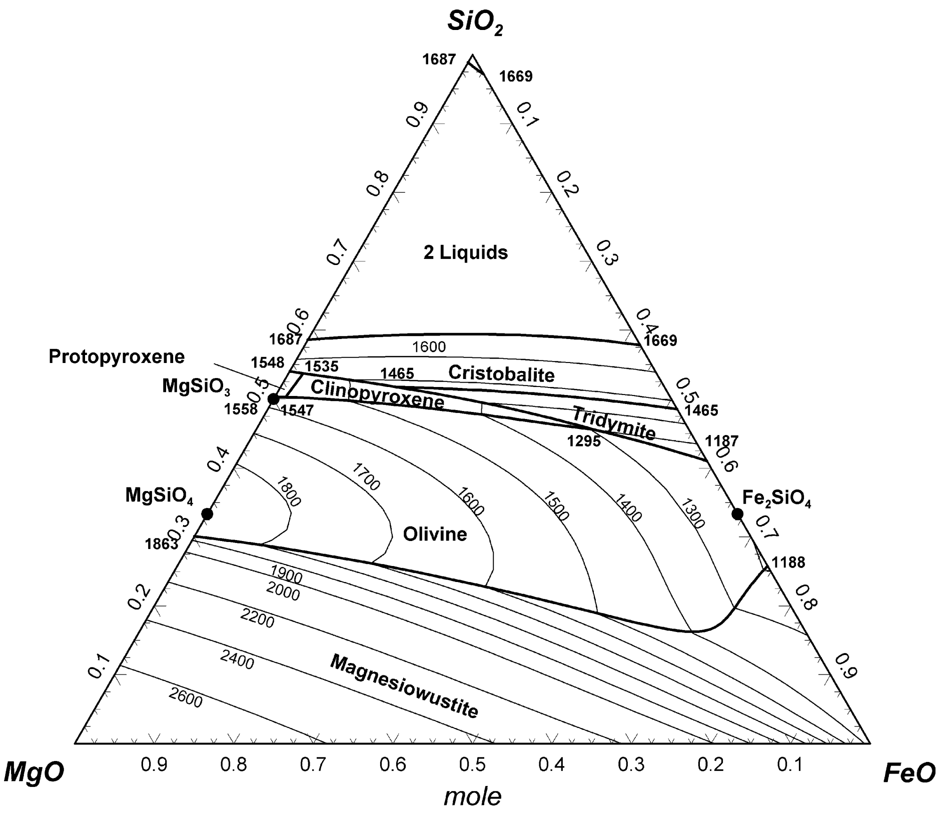

Fig. 2 Calculated liquidus projection of the FeO-Fe_2O_3-MgO-SiO_2 system at 1 bar total pressure in equilibrium with metallic iron. The thin solid lines are calculated isotherms; temperatures are in °C. The univariant lines are bold. (Projection from the Fe-corner of the Fe-FeO-MgO-SiO_2 tetrahedron onto the basal plane)

Several other components, MnO, CrO, Cr_2O_3, NiO, CoO, etc., have been added to the six-component system, Al_2O_3-CaO-FeO-Fe_2O_3-MgO-SiO_2, over the range of composition, temperature, and oxygen partial pressure which is important for ferrous process metallurgy. In particular, the Al_2O_3-CaO-MnO-SiO_2 system has been optimized.[21-23] This system is of interest for inclusion control in Mn/Si-killed steel as will be discussed in more detail in the following sections. The phase equilibria in this quaternary system are illustrated in Fig. 6 to 13. The optimized phase diagrams for the MnO-CaO and MnO-SiO_2 binary subsystems have been published elsewhere.[24,25] These figures demonstrate how thermodynamic models simultaneously describe phase diagrams (Fig. 6 and 10), thermodynamic properties (Fig. 7), activities (Fig. 8 and 11), and slag-alloy phase equilibria (Fig. 12). Of course, a great number of other experimental data points have also been reproduced. Figures 9 and 13 present the calculated phase diagrams of all ternary subsystems and one section through the quaternary system, which are consistent with thermodynamic laws and with all experimental information available for this quaternary system. Similarly, the thermodynamic databases which have been developed make it possible to calculate any other phase diagram section even for regions of composition and temperature where no experimental data are available.

A new model and database to calculate the viscosity of silicate melts has been developed.[42,43] The model relates the viscosity to the structure of the melt, and the structure in turn is calculated from the thermodynamic description of the melt using the Modified Quasichemical Model. Parameters of the viscosity model were optimized for the system Na_2O-K_2O-MgO-CaO-MnO-FeO-ZnO-PbO-Al_2O_3-SiO_2. The model describes all binary MeO_x-SiO_2 systems within experimental uncertainty, using one or two binary viscosity parameters per system. In addition, two ternary parameters are needed for every MeO_x-Al_2O_3-SiO_2 system to account for a viscosity maximum that arises due to the "charge compensation effect" when Al cations assume tetrahedral coordination against oxygen and replace Si in the silica network while the missing charge is compensated by a Me ion that stays close to the Al ion. The viscosities of multicomponent systems are then predicted by the model without introducing any additional parameters. The viscosity database is being expanded to include all components of the liquid slag in the FACT oxide database so that whenever the slag appears in a phase equilibrium calculation, its viscosity will also be calculated.

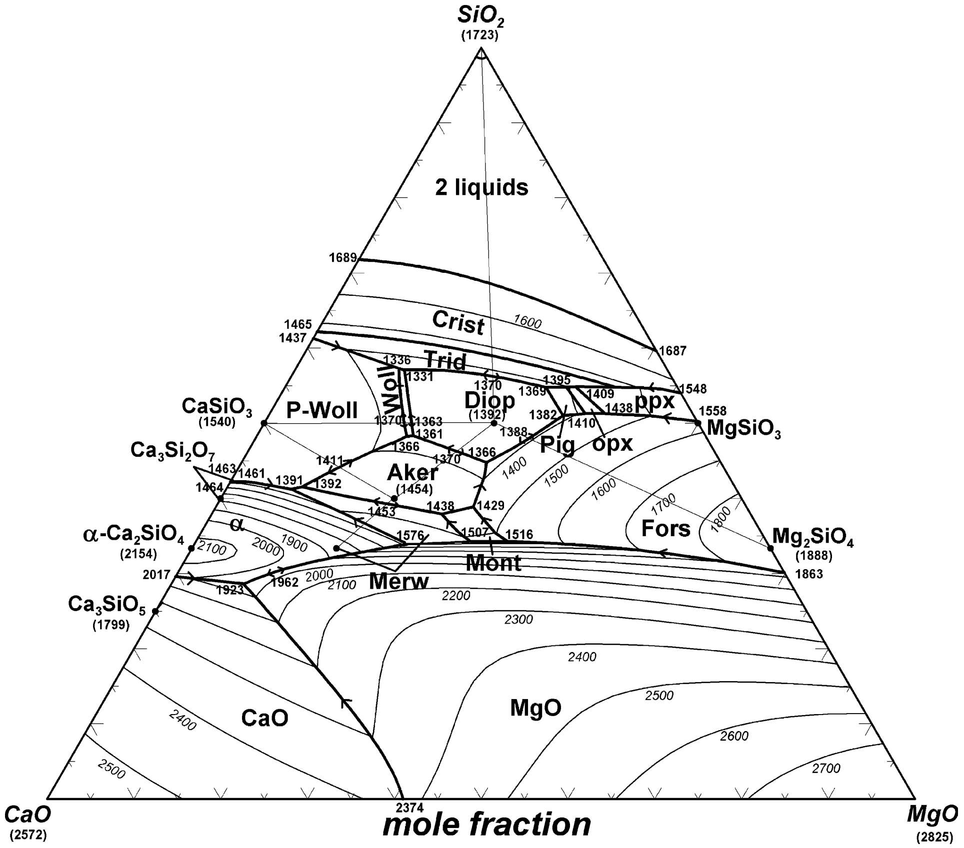

Fig. 3 Calculated (optimized) liquidus surface of the CaO-MgO-SiO_2 system at 1 bar pressure. Temperatures in °C. Phase names are: Tridymite (Trid), Cristobalite (Crist), Pseudo-wollastonite (P-Woll), Wollastonite (Woll), Diopside (Diop), Pigeonite (Pig), Ortho-pyroxene (opx), Proto-pyroxene (ppx), Akermanite (Aker), Forsterite (Fors), Monticellite (Mont), and Merwinite (Merw)

4. Thermodynamic Calculations in Refining Processes

4.1 Hydrogen in Steels and Water Capacity of Molten Slags

Hydrogen is one of the most harmful gaseous species for steels. It causes notorious hydrogen-induced cracking (HIC), embrittlement, and pores in steels. The most adequate way to remove hydrogen from liquid steel is a vacuum degassing treatment. Dehydrogenation kinetics is greatly influenced by top slags during this process. However, since the hydrogen content in steel is usually reduced below the refining limit of top slags during the treatment, hydrogen can be picked-up from top slags after the degassing process. Therefore, it is important to model the solubility of water in slags to improve the control of hydrogen in steels.

Water dissolves in molten slags as hydroxyl ions or hydroxyl radicals depending on slag basicity. In basic slags, water vapor reacts with free oxygen ions to form hydroxyl ions:

$$O^{2-} + H_2O = 2OH^-$$

In acidic slags, on the other hand, water vapor reacts with "bridging" oxygen (oxygen covalently bonded to two silicon atoms) and breaks the silica network to form hydroxyl radicals according to the following reaction:

$$(-\overset{|}{\underset{|}{\mathrm{Si}}}-\mathrm{O}-\overset{|}{\underset{|}{\mathrm{Si}}}-) + \mathrm{H_2O} = -\overset{|}{\underset{|}{\mathrm{Si}}}-\mathrm{OH} + \mathrm{HO}-\overset{|}{\underset{|}{\mathrm{Si}}}-$$

Because of these different dissolution mechanisms, the solubility of water in molten slags passes through a minimum with the variation of the slag basicity due to the change in the amount of free oxygen ions and oxygen bridges available for reactions with water.

In general, the water capacity is defined as

$$C_{\mathrm{OH^-}} = \frac{(\mathrm{wt.\%\ H_2O})}{\sqrt{P_{\mathrm{H_2O}}}}$$

The dissolution of water in oxide melts is modeled by an integration of the capacity model[8] which describes the solubility of hydroxyl ions and the Modified Quasichemical Model[2-4,44] which incorporates H_2O as an oxide component of the melt to account for the solubility of hydroxyl radicals. The details of the model and model parameters can

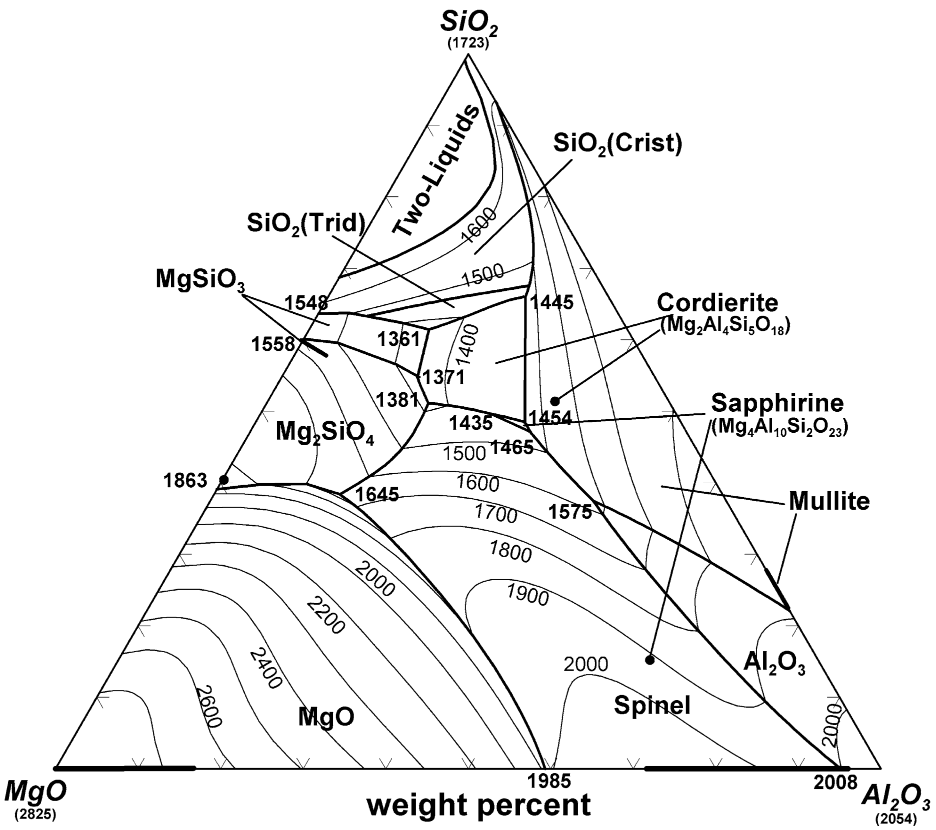

Fig. 4 Calculated liquidus surface of the MgO-Al_2O_3-SiO_2 system. Temperatures in °C

be found elsewhere.[45,46] The model parameters were optimized to reproduce reliable experimental data on the water capacity of various molten slags.

The calculated water capacities of the Al_2O_3-CaO-MgO-SiO_2 metallurgical slags are shown in Fig. 14 to 16. As can be seen from Fig. 14, the water capacity has a minimum at about 50 wt.% SiO_2 and 25 wt.% CaO and Al_2O_3. The addition of MgO to the slag results in slight increase of the water capacity, but the shape of iso-capacity lines remains the same as shown in Fig. 15.

Figure 16 shows the effect of temperature and slag composition on water capacity in the Al_2O_3-CaO-MgO-SiO_2 slags. The model predicts that the water capacity decreases with an increasing temperature. Dash-dotted and solid lines show the variation of the water capacity in the Al_2O_3-CaO-SiO_2 and Al_2O_3-CaO-MgO-SiO_2 slags, respectively, as a function of Al_2O_3 concentration. The water capacity of the slags decreases drastically with the increase in Al_2O_3 content. On the other hand, the replacement of CaO by MgO in the Al_2O_3-CaO-MgO-SiO_2 slag at constant slag basicity can slightly increase the water capacity as can be seen from the dashed lines.

A similar hybrid model has been also developed for dissolution of carbon and nitrogen in molten slags,[45,46] and the results can be readily used for calculations related to control of these elements in steel.

4.2 Phosphorus Control in Steelmaking

Phosphorus is usually a detrimental impurity in steel affecting its mechanical properties. In particular, P is mainly responsible for brittleness of steel. It precipitates along grain boundaries and lowers the strength and ductility at high temperatures. Therefore, P is usually controlled below 0.1 wt.% during refining of steel.

The source of P in steel is iron ore which contains a small amount of P_2O_5. This P_2O_5 is reduced during the ironmaking process in a blast furnace and is dissolved in pig iron. Thereafter, the reduced P is removed to top slag by injecting some fluxes such as $CaCO_3$ during hot metal pretreatment and/or converting. Therefore, thermodynamic modeling of P in molten iron and slag is important to improve control of the P level in steel.

Thermodynamic behavior of P in molten Fe is characterized by strong negative deviations from ideality as can be seen from calorimetric[47] and activity[48] measurements. The strong interactions between Fe and P are not well described by the models which assume random mixing of atoms, such as the well-known interaction parameter formalism of Wagner[49] or the Bragg-Williams model. In this study, an associate "FeP" was introduced in liquid iron to mix randomly with free "Fe" and free "P" species. As can be seen from Fig. 17(a) and (b), the associate model

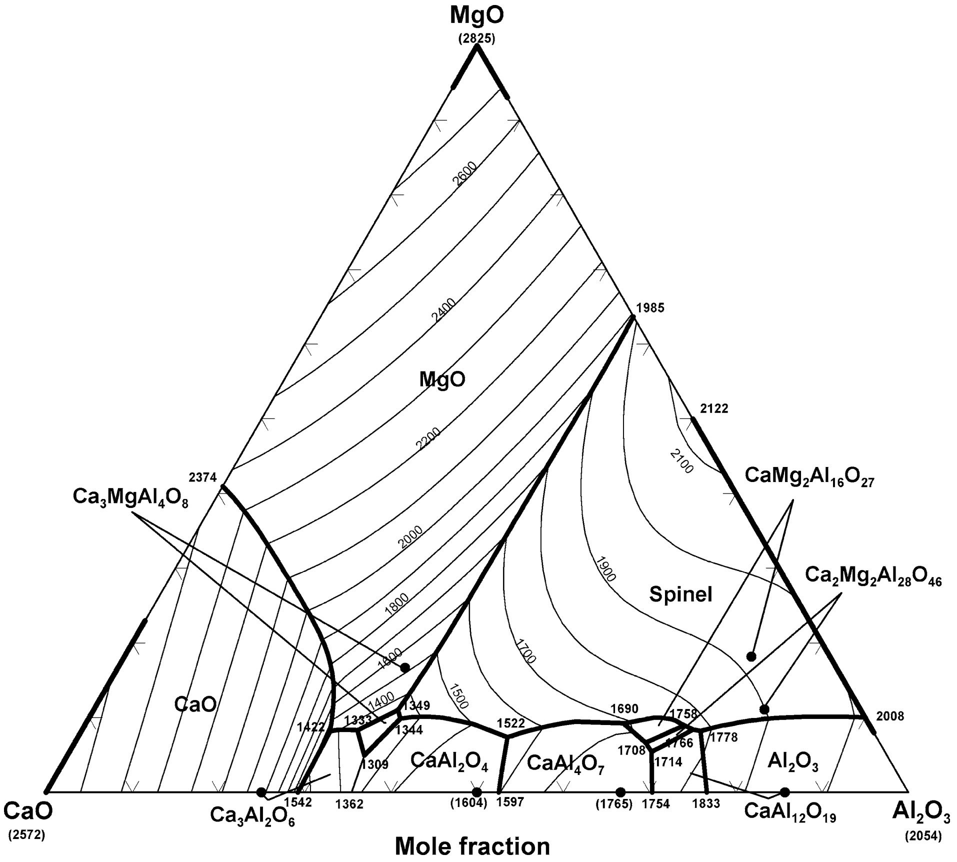

Fig. 5 Calculated liquidus projection of the CaO-MgO-Al_2O_3 system. Temperatures in °C

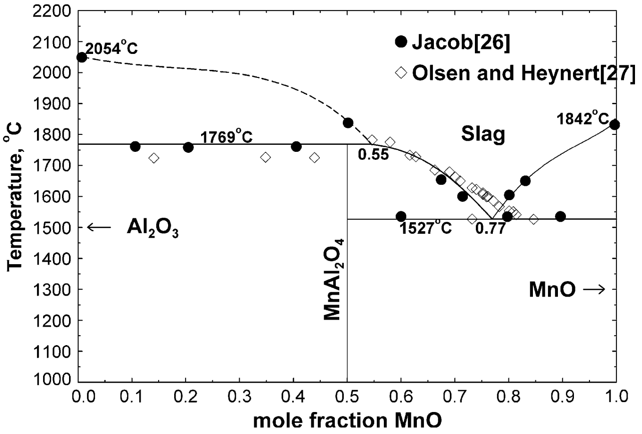

Fig. 6 Calculated (optimized) MnO-Al_2O_3 phase diagram

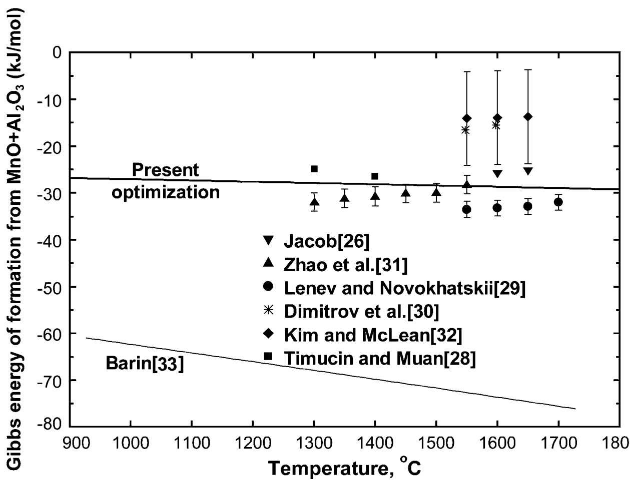

Fig. 7 Optimized Gibbs energy of formation of $MnAl_2O_4$ from solid MnO and Al_2O_3

gives a better description of thermodynamic properties of the Fe-P liquid alloy than the random mixing model.

In liquid slag, P_2O_5 exhibits very strong interactions with basic oxides such as CaO, MgO, FeO, etc. In this study, this is taken into account by using the Modified Quasichemical Model in the pair approximation.[3] P_2O_5 dissolves in the slag by forming phosphorus tetrahedra (PO_4^{3-}). Furthermore, two such tetrahedra can be linked together by sharing one bridging oxygen (i.e., $P_2O_7^{4-}$). Since the Raman spectroscopy study[50] indicated that the amount of these double phosphorus tetrahedra is much higher than that of the single phosphorus tetrahedra, it was assumed that the actual component of the slag is "P_2O_5" rather than "$PO_{2.5}$". Only the slags containing less than

30 wt.% P_2O_5 were considered because P_2O_5 is very volatile at high temperatures and it is difficult to obtain reliable experimental data in the P_2O_5-rich region. However, this range is sufficient for practical applications related to dephosphorization of steel.

Banya and Watanabe[51] reported the oxygen partial pressure in an H_2O-H_2 gas mixture equilibrated with a FeO-Fe_2O_3-P_2O_5 slag and solid iron. As can be seen from Fig. 18, the equilibrium oxygen partial pressure decreases when the concentration of P_2O_5 increases in the slag. This can be easily understood considering the equilibrium constant of the reaction[51]

$$\mathrm{Fe\,(solid) + 1/2O_2\,(gas) = FeO\,(slag)}$$

and taking into account that the activity of FeO decreases with an increasing P_2O_5 concentration because of strong interactions between FeO and P_2O_5. The small systematic differences between the calculated lines and the experimental points originate from a slight inconsistency of the latter with our thermodynamic description of the Fe-O system which is based on numerous experimental data.

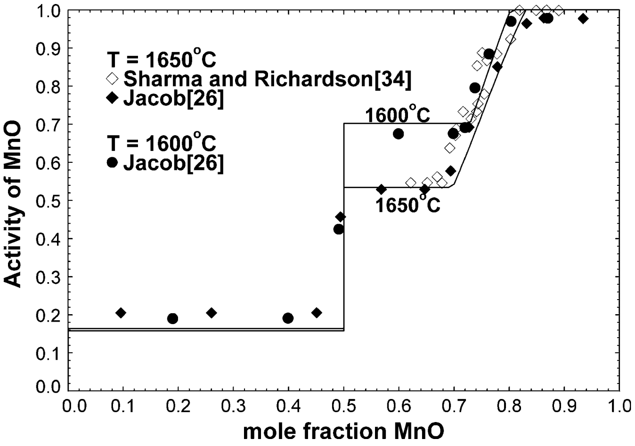

Fig. 8 Calculated (optimized) activity of MnO (with respect to solid standard state) in the MnO-Al_2O_3 system at 1600 and 1650 °C

The distribution of P between molten iron and the CaO-saturated CaO-FeO-Fe_2O_3-P_2O_5 slag is shown in Fig. 19. Experimental data by Nagabayashi et al.[52] at three different temperatures are compared with the calculations based on our thermodynamic models for the dissolution of P in liquid iron and slag. The P distribution ratio decreases with an increasing temperature and exhibits a peculiar dependence on iron concentration passing through a maximum as the iron content in the slag increases. This can be explained by a combined effect of FeO and CaO during the dephosphorization process. The initial increase of the amount of ($FeO + Fe_2O_3$) in the slag provides oxygen for oxidizing P from liquid Fe to form P_2O_5 in the slag. However, this also

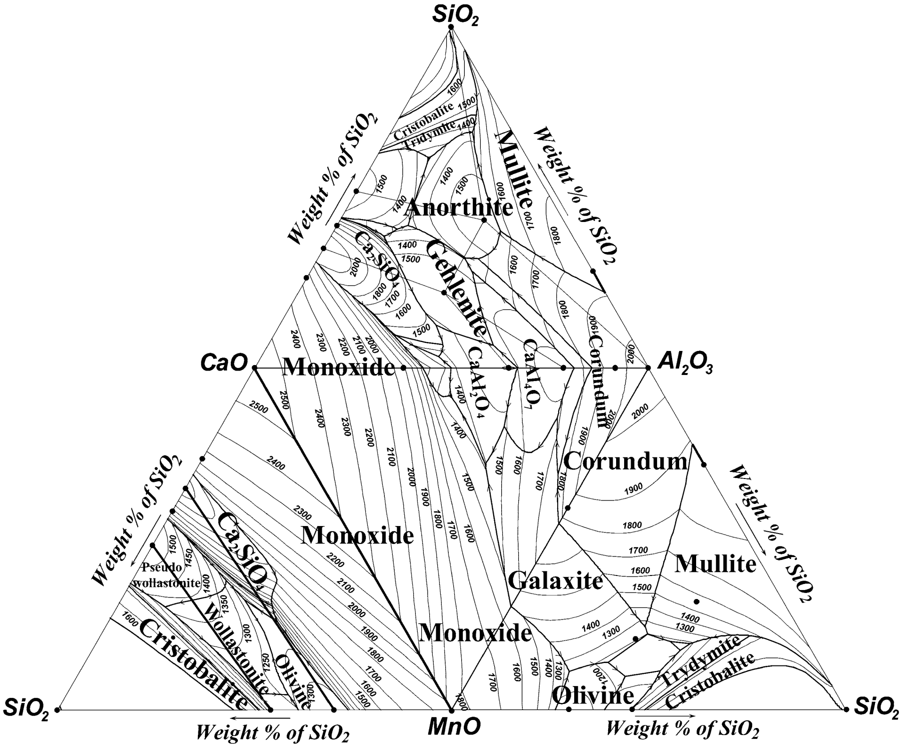

Fig. 9 Liquidus surfaces of the four ternary subsystems of the Al_2O_3-CaO-MnO-SiO_2 system calculated from the thermodynamic models (Temperature in °C)

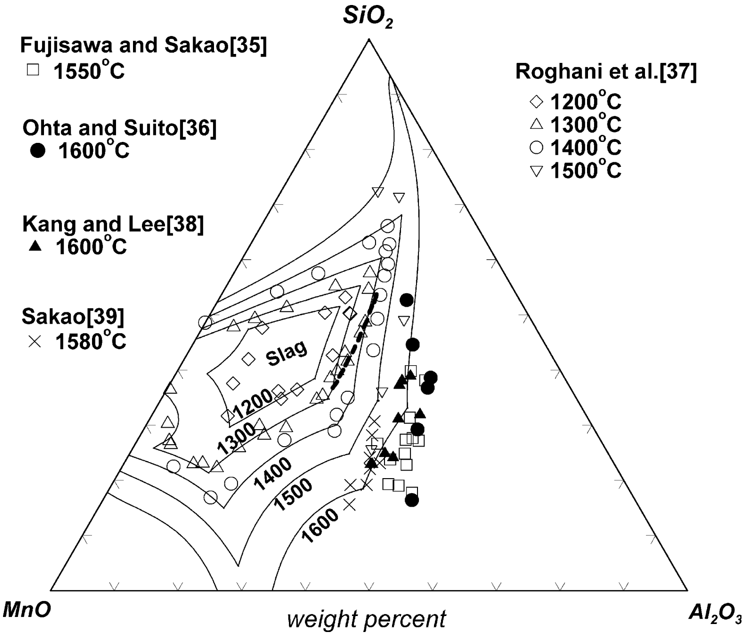

Fig. 10 Calculated liquidus of the Al_2O_3-MnO-SiO_2 system at temperatures between 1200 and 1600 °C compared with experimental data. Dashed line is calculated metastable liquidus of Al_2O_3 (corundum) at 1300 °C

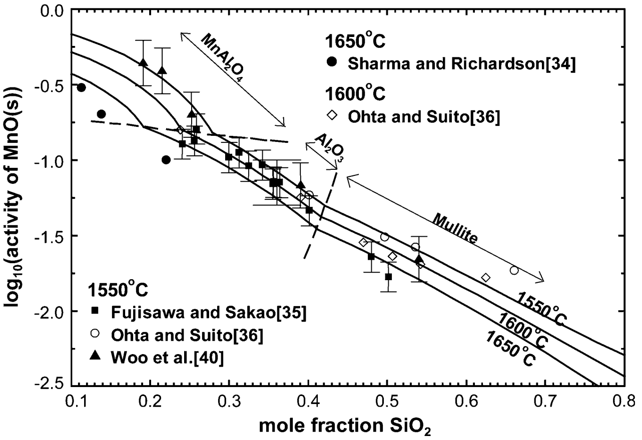

Fig. 11 Calculated activities of MnO (solid standard state) in Al_2O_3-MnO-SiO_2 liquid slags at 1550, 1600, and 1650 °C at saturation with solid $MnAl_2O_4$, Al_2O_3, or Mullite

decreases the concentration of CaO in the slag and eventually results in the decrease of the P distribution ratio because P_2O_5 is stabilized in the slag due to particularly strong interactions between CaO and P_2O_5 which are much stronger than the interactions between FeO and P_2O_5. As can be seen from Fig. 19, the calculations reproduce well both the temperature and the concentration dependence of the P distribution ratio.

4.3 Ca Deoxidation: The Fe-Ca-O System

Figure 20 shows the calculated deoxidation curve in the Fe-Ca-O system at 1600 °C compared with experimental data.[53-58] According to the Associate Model,[9] which is used for liquid steel in the FactSage steel database, it is assumed that liquid steel contains dissolved unassociated Ca and O atoms as well as molecules (associates) CaO. The curves in Fig. 20 were calculated using the Associate Model with one temperature-independent parameter, which is the Gibbs energy Δg_{CaO} for the association reaction Ca + O = CaO.

The shape of the calculated Ca deoxidation curve in Fig. 20 may be explained as follows. Because Δg_{CaO} is very negative, the association reaction is displaced very strongly to the right. Hence, a solution will contain either dissolved CaO and O species (but virtually no Ca species) or dissolved CaO and Ca species (but virtually no O species). Suppose we start with liquid steel containing a high concentration of dissolved oxygen at 1600 °C and begin adding Ca. At first, the Ca reacts with the oxygen to form CaO associates, leaving virtually no free Ca in solution. When the concentration of CaO reaches ~17 ppm, it attains equilibrium with solid CaO: CaO = CaO(s).

As more Ca is added to the liquid steel, it reacts with dissolved oxygen to precipitate solid CaO; the concentration of dissolved oxygen thus decreases, while the concentration of CaO remains constant (and hence the concentration of total dissolved Ca remains nearly constant). This results in the nearly vertical section of the deoxidation curve in Fig. 20. When the total dissolved oxygen content has been reduced to ~5 ppm, the concentrations of free dissolved O and Ca are both extremely low, and CaO associates are virtually the only species in the liquid steel solution which is saturated with CaO solid. Further addition of Ca thus serves only to increase the free Ca concentration, with virtually no further precipitation of CaO; hence, the nearly horizontal section of the curve in Fig. 20.

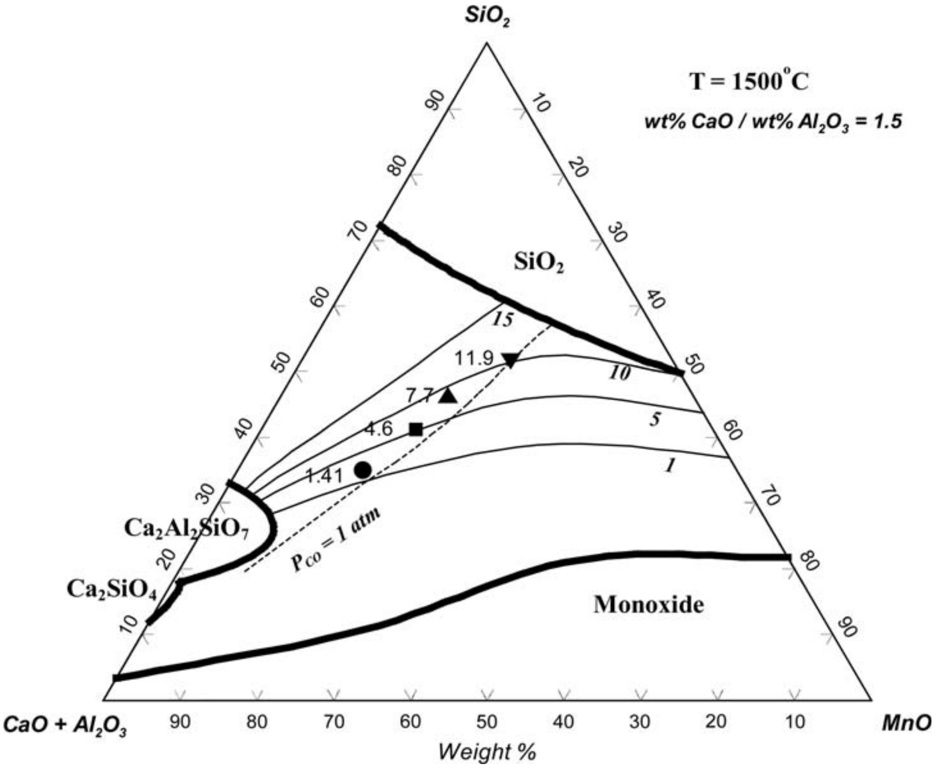

Fig. 12 Calculated composition of Al_2O_3-CaO-MnO-SiO_2-(FeO) liquid slag with a CaO/Al_2O_3 weight ratio of 1.5 in equilibrium with C-saturated Fe-Mn-Si-C alloy containing 11 wt.% Fe and indicated constant weight percent Si at 1500 °C. Dashed line is the calculated composition of the liquid slag in equilibrium with the manganese alloy and a gas phase with $P_{CO} = 1$ atm. Experimental points of Ding and Olsen[41] at $P_{CO} = 1$ atm are also shown. The calculated FeO content of the slag is <0.01 wt.%

Several authors[53,54,59-62] have attempted to model the Ca deoxidation curve using the classical Wagner formalism without considering the formation of associates. Very large negative temperature-dependent first- and second-order interaction parameters ε^{O}_{Ca}, ρ^{O}_{Ca}, $\rho^{Ca,O}_{Ca}$ were required. Furthermore, most authors also had to arbitrarily adjust the equilibrium constant K_{CaO} for the formation of solid CaO by two or three orders of magnitude from its literature value to fit the data. In the present calculations, this was not necessary, and accepted literature values were used as recommended by Turkdogan.[63] The calculated solubility (deoxidation) curves by other authors all have strange shapes, some with minima and maxima, and even one in the form of a circle.[54] The model of JSPS[59] is the most widely used; the “deoxidation curve” calculated from such a model, and reported in the literature, is shown in Fig. 20 by the dashed line. We have shown[9] that the dashed line actually represents an unstable solution of the interaction parameter formalism in the JSPS model, and its true stable solution actually lies at extremely low (<0.01 ppm) Ca and O contents. Hence, we believe that the present calculations elucidate the deoxidation behavior of Ca for the first time.

4.4 Al Deoxidation: The Fe-Al-O System

The deoxidation curves from several selected authors[64-69] are shown in Fig. 21. According to the Associate Model,[9] which is used for liquid steel in the FactSage steel database, it is assumed that liquid steel contains dissolved unassociated Al and O atoms as well as associates AlO and Al_2O.

In a very dilute liquid steel solution, unassociated Al and O predominate. Therefore, the deoxidation reaction may be written as $2Al + 3O = Al_2O_3(solid)$. From the equilibrium constant of this reaction, one would expect the oxygen content to decrease continuously as the dissolved Al content increases. This is indeed the case for low Al contents where most of the oxygen is dissolved as free O.

However, at higher Al contents, most of the dissolved oxygen is in the form of AlO associates because the equilibrium constant of association reaction $Al + O = AlO$ is very large, and the principal deoxidation equilibrium becomes $3AlO = Al_2O_3(solid) + Al$. From the equilibrium constant of this reaction, one can deduce that an increase in the total dissolved Al content now results in an increase in X_{AlO} and thus an increase in total dissolved oxygen. Hence, a “deoxidation minimum” is observed in the curves of Fig. 21. Note that the axes in Fig. 21 give the total dissolved Al (as $Al + AlO + 2Al_2O$) and the total dissolved oxygen (as $O + AlO + Al_2O$). Therefore, in general, if the Gibbs energy of formation for an associate is sufficiently negative, a deoxidation minimum will be observed for a deoxidant M whenever the deoxidation product M_xO_y has a ratio $(y/x) > 1$.

The Gibbs energies of association reactions $Al + O = AlO$ and $2Al + O = Al_2O$ were optimized to reproduce the

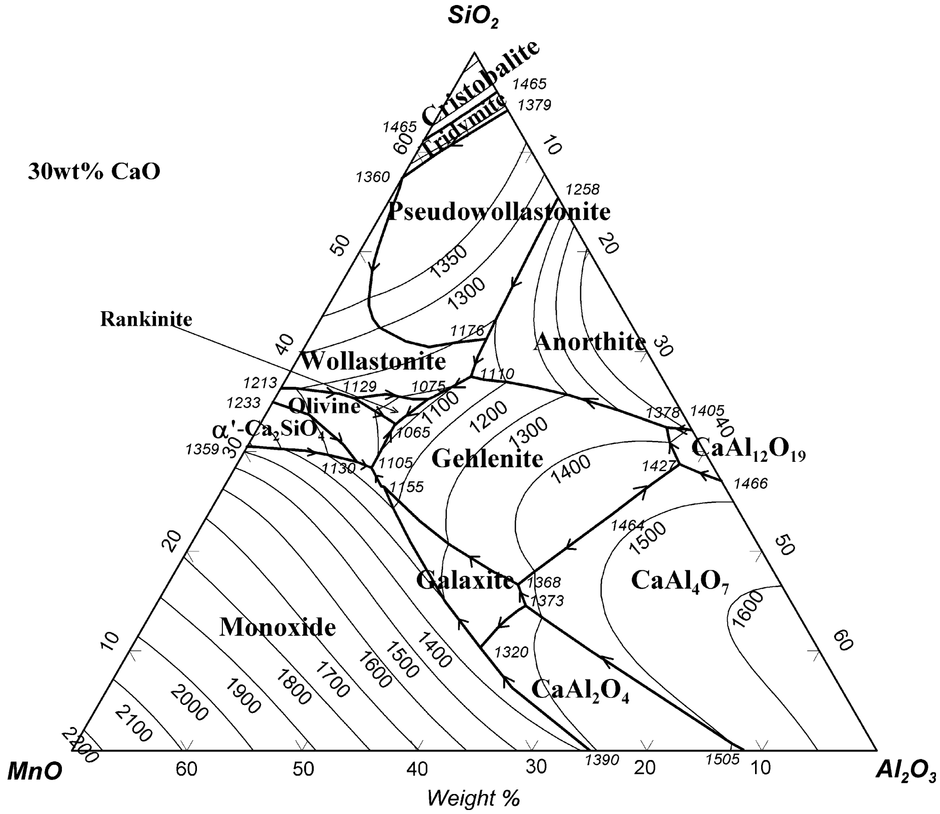

Fig. 13 Predicted liquidus surface of the Al_2O_3-CaO-MnO-SiO_2 system at 30 wt.% CaO

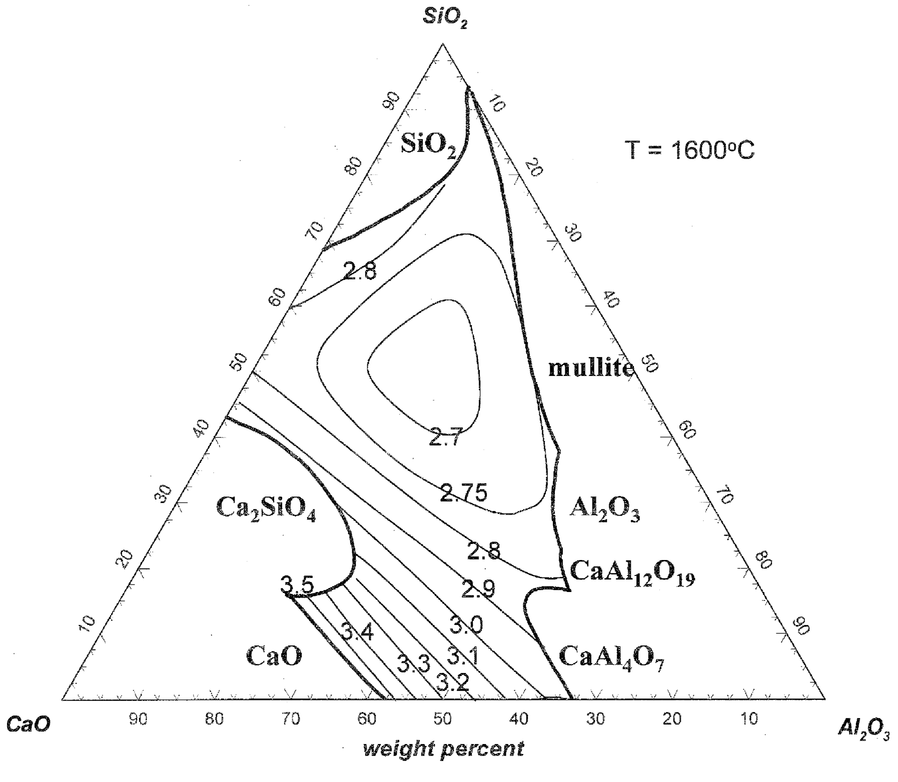

Fig. 14 Predicted iso-capacity lines showing the solubility of water in the Al_2O_3-CaO-SiO_2 slag at 1600 °C. The numbers are $\log_{10}(C_{OH^-} \times 10^4)$

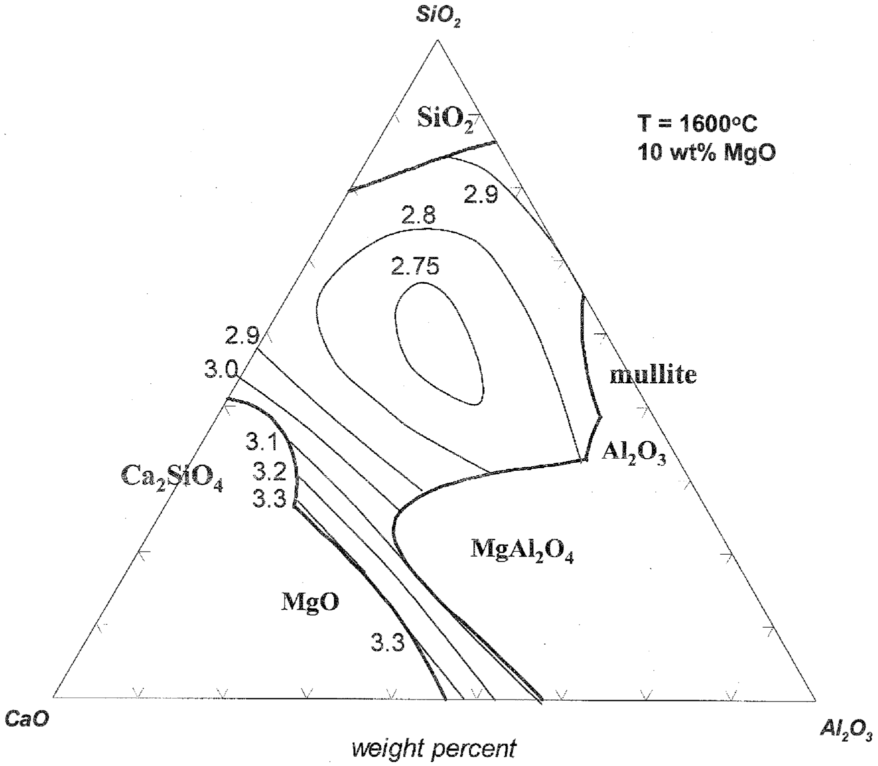

Fig. 15 Predicted iso-capacity lines showing the solubility of water in the Al_2O_3-CaO-10 wt.%MgO-SiO_2 slag at 1600 °C. The numbers are $\log_{10}(C_{OH^-} \times 10^4)$

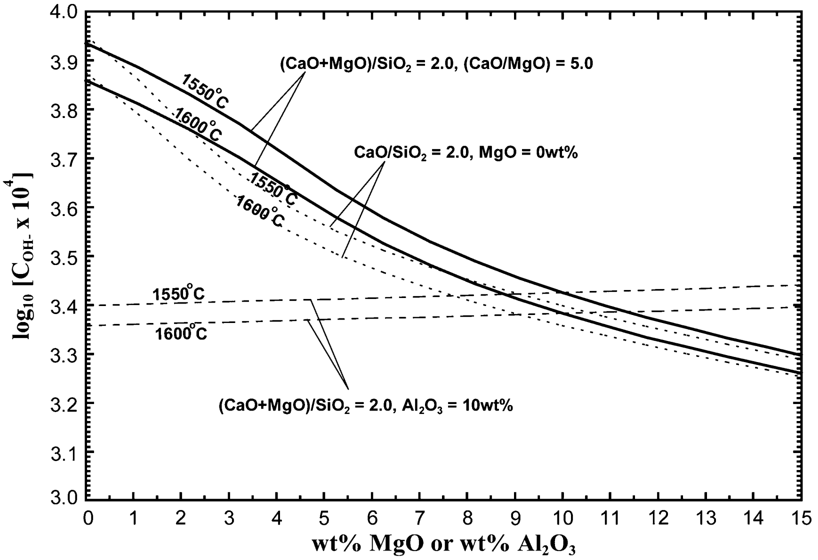

Fig. 16 Predicted water capacity for molten Al_2O_3-CaO-MgO-SiO_2 slags at 1550 and 1600 °C

experimental data. The curves in Fig. 21 are calculated from these parameters. Although the parameters are constant, independent of temperature, the temperature dependence of the $[Al]_{total} - [O]_{total}$ data in liquid steel is very well reproduced by the model.

It can easily be shown that the assumption of the higher associate Al_2O only has a visible effect on the calculated curves when log[wt.% total Al] > −0.3. Even at higher Al concentrations, an acceptable fit can be obtained without considering the formation of Al_2O.

Previously, Sigworth and Elliott[70] modeled this system using the Wagner interaction parameter formalism without considering the formation of such Al-O associates. A very negative parameter ε_{Al}^{O} was required, with a temperature

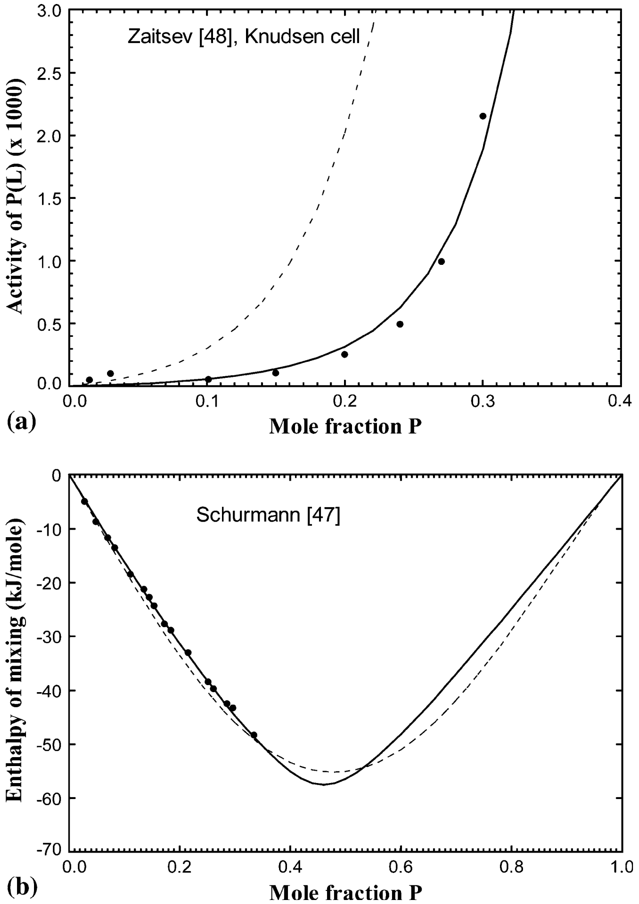

Fig. 17 Calculated thermodynamic properties of the Fe-P binary liquid, compared with available experimental observations. Solid and dashed lines are calculated using the models from this work and the subregular model, respectively. (a) Activity of P relative to pure liquid P. (b) Enthalpy of mixing

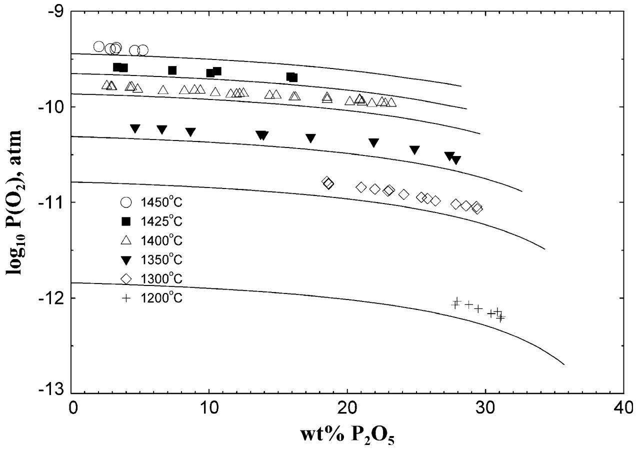

Fig. 18 Oxygen partial pressures over the FeO-Fe_2O_3-P_2O_5 slag in equilibrium with solid Fe. Points represent experimental measurements by Banya and Watanabe[51] for the equilibrium between H_2O-H_2 gas, solid Fe, and FeO-Fe_2O_3-P_2O_5 slag

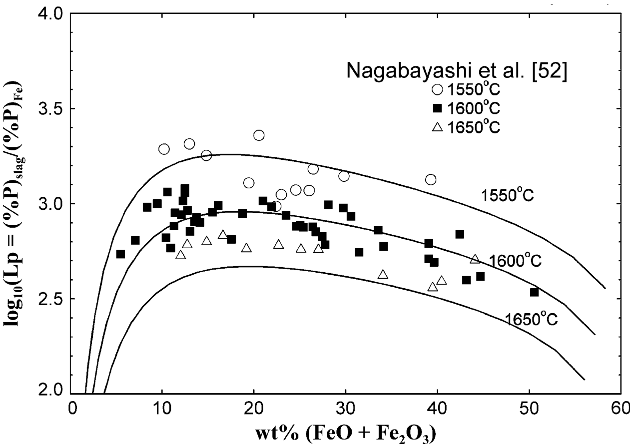

Fig. 19 Phosphorus distribution ratio: wt.% P in the CaO-saturated CaO-FeO-Fe_2O_3-P_2O_5 slag divided by wt.% P in liquid steel. Experimental points[52] and calculated lines

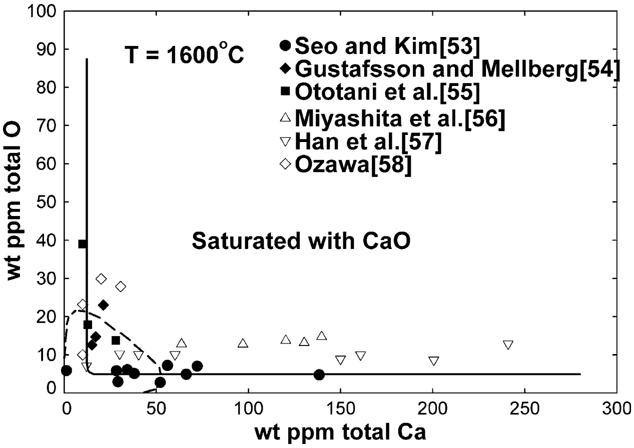

Fig. 20 Total dissolved oxygen and total dissolved Ca contents of liquid steel in equilibrium with solid CaO. Lines are calculated from the liquid steel database with the Associate Model.[9] Dashed line is calculated from Wagner formalism with parameters of JSPS[59]

dependence chosen to fit the data. The deoxidation equilibrium at 1600 °C, calculated by their model, is shown in Fig. 21 by the dashed line. Clearly, their model cannot be extrapolated outside the composition range of the data. On the other hand, with the present model, extrapolations both in composition and temperature are reasonable.

5. Applications of Thermodynamic Databases to Inclusion Engineering

Inclusion control is the key to the production of high clean or ultrahigh clean steel. Inclusions appear in steel at various stages of its production and cause serious

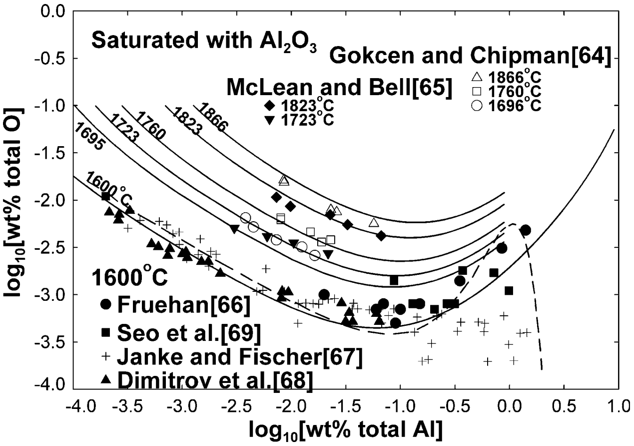

Fig. 21 Total dissolved oxygen and total dissolved Al contents of liquid steel in equilibrium with solid Al_2O_3. Lines are calculated from the liquid steel database with the Associate Model.[9] Dashed line is calculated from Wagner formalism with parameters of Sigworth and Elliott[70]

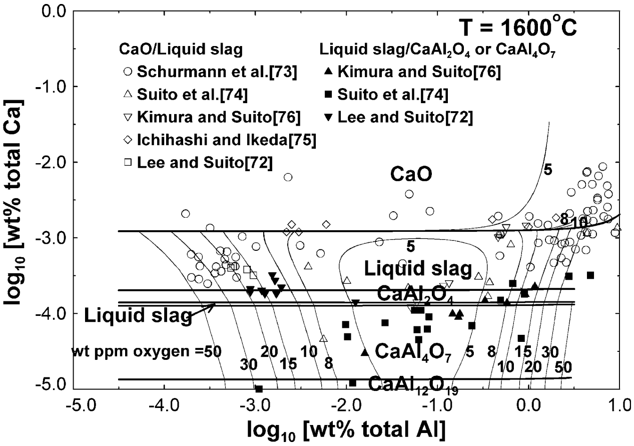

Fig. 22 Calculated inclusion diagram for complex deoxidation with Ca and Al showing total dissolved oxygen content of liquid steel and equilibrium deoxidation products as functions of total dissolved Ca and Al

problems: nozzle clogging, breakage of steel wire during drawing, HIC, low-temperature embrittlement, fatigue failure, degradation of surface quality, and so on. Inclusions are mainly formed either during the deoxidation process, or by slag entrapment, breakdown of refractory materials, and reoxidation by air. Inclusions can also precipitate due to changes of solubility which occur as temperature decreases.

Inclusions can be floated and captured by top slags in secondary steelmaking processes. However, the removal of inclusions is very limited during these processes due to the short process time and to the continuous circulation of liquid steel in the ladle. Therefore, the control of the composition of inclusions has become crucial in modern steelmaking processes. That is, since the presence of inclusions cannot be avoided, it is important to modify their composition to render them less harmful. Because, thermodynamically, the composition of inclusions is very sensitive to the concentrations of even dilute elements dissolved in the steel, accurate thermodynamic data for both steel and inclusions are indispensable to the development of inclusion engineering technology.

In this section, a few examples will be presented to demonstrate the versatility and accuracy of the thermodynamic databases which have been developed for calculations of importance to inclusion engineering. Some additional examples have recently been reported by Jung et al.[71]

5.1 Modification of Solid Al_2O_3 Inclusions to Liquid CaO-Al_2O_3 Inclusions: The Fe-Al-Ca-O System

Solid Al_2O_3 inclusions formed during the Al deoxidation process are not easily removed by floating in the secondary refining process, and thereafter they may degrade the mechanical properties of the steel as well as cause nozzle clogging. To reduce these harmful effects, Ca treatment technology is often used, by which solid Al_2O_3 inclusions are modified to less harmful liquid CaO-Al_2O_3 inclusions. The globular liquid inclusions can float more easily to the top slag in the secondary steelmaking process and are less likely to become attached to the nozzle wall. To understand the Ca treatment process, an inclusion diagram for the Fe-Al-Ca-O system is essential.

Figure 22 presents the inclusion diagram for the Fe-Al-Ca-O system at 1600 °C calculated using the thermodynamic databases. The equilibrium deoxidation products are also indicated on the diagram and the phase boundaries are represented as heavy lines. Iso-oxygen content lines from 5 to 50 wt. ppm oxygen are also plotted. Each point on the diagram represents an equilibrium of liquid steel with one or two oxide phases. That is, if oxygen is progressively dissolved in the liquid iron containing certain amounts of Al and Ca (as given by the axes of the diagram), then an oxide phase indicated on the diagram will precipitate when a certain oxygen content is reached. The latter can be estimated from the iso-oxygen lines. Since the oxide phases contain a very small amount of iron under these conditions, their compositions are close to the CaO-Al_2O_3 system. As can be seen from Fig. 23, there are two slag regions at 1600 °C on both sides of the $CaAl_2O_4$ compound. Since $CaAl_2O_4$ melts congruently at ~1604 °C, a similar diagram calculated above 1604 °C would not contain the $CaAl_2O_4$ region. Similarly, since the $CaAl_2O_4$-$CaAl_4O_7$ eutectic temperature is ~1596 °C, a diagram calculated below 1596 °C would not contain the lower "Liquid slag" region.

A deoxidation minimum is clearly seen near log [wt.% Al] ~ -1.2 (i.e., at Al concentration of about 500 wt. ppm) similar to Fig. 21. It can be seen that the equilibrium deoxidation product is nearly independent of Al content, depending only on the Ca content. When log[wt.% total Ca] > -2.9 (i.e., total dissolved Ca > 13 ppm), solid CaO is the deoxidation product, and the oxygen content is ~5 wt. ppm. At higher total Ca contents, the oxygen content does not decrease substantially below 5 ppm. This behavior can be understood with reference to the Ca deoxidation curve in the Fe-Ca-O system in Fig. 20, where the nearly vertical and

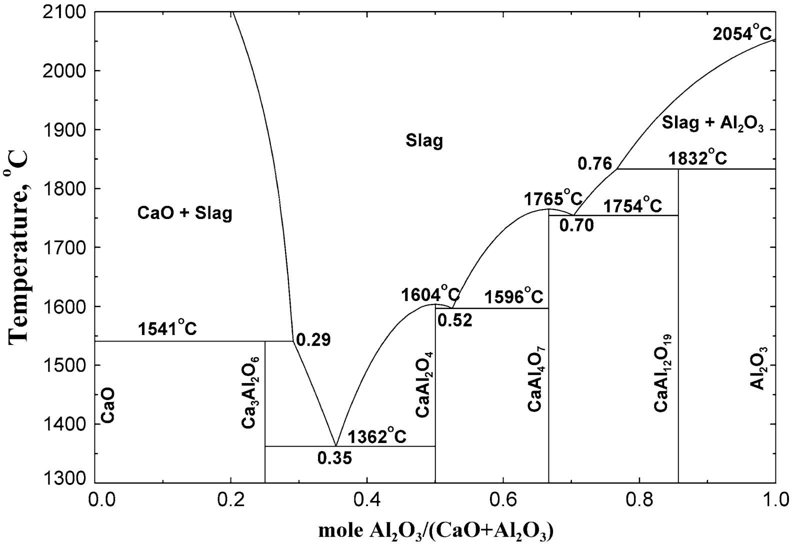

Fig. 23 Calculated (optimized) CaO-Al_2O_3 phase diagram

nearly horizontal branches of the deoxidation curve occur at ~13 wt. ppm Ca and ~5 wt. ppm O, respectively. In particular, the drastic change of the oxygen content in the steel after crossing the CaO + Slag equilibrium line at about 13 wt. ppm Ca corresponds to the nearly vertical line in Fig. 20.

Several authors[72-76] have measured the line along which solid CaO and liquid slag co-exist as well as the line along which either (slag + $CaAl_2O_4$) or (slag + $CaAl_4O_7$) co-exist. Measurements were performed in CaO crucibles in the first case, and Al_2O_3 crucibles in the second case. The data points are plotted in Fig. 22. Within the large experimental scatter, these results confirm the model calculations.

Our newly calculated inclusion diagram differs significantly from those previous diagrams,[53,77-80] in which the presented phase boundaries slope upwards to the right.

The inclusion diagram can be applied to the Ca-treatment of Al_2O_3 solid inclusions. To modify the Al_2O_3 inclusions to the liquid CaO-Al_2O_3 phase, at least ~2 wt. ppm Ca (i.e., log [wt.% Ca] ~ -3.7) is necessary, but the Ca content should be less than ~13 wt. ppm (log [wt.% Ca] ~ -2.9) to prevent the formation of the solid CaO phase. It should be noted that although the Ca treatment for Al_2O_3 inclusions is useful to prevent nozzle clogging and to absorb inclusions in top slags, the lowest eutectic temperature in the CaO-Al_2O_3 binary system is still much higher than the temperature in the rolling process. Therefore, the CaO-Al_2O_3 inclusions will be solid and undeformable during the rolling process.

5.2 Formation of CaS Inclusions During Ca Treatment: The Fe-Al-Ca-Si-O-S System

During the Ca treatment process discussed above, the amount of sulfur in the liquid steel is very important because solid CaS is readily formed. CaS inclusions can be as harmful as solid Al_2O_3. Therefore, the Ca/S ratio in liquid steel should be closely controlled.[81]

Figure 24 shows the calculated results for the simulation of CaSi(1:1) wire injection into 100 tonnes of liquid steel (iron containing 6, 30, and 500 wt. ppm O, S, and Al, respectively) with suspended Al_2O_3 inclusions. In the calculations, no losses of CaSi (as, for example, by the volatilization of Ca) are assumed. The amount of suspended Al_2O_3 inclusions is set at 100 wt. ppm in Fig. 24(a) and 300 wt. ppm in Fig. 24(b). As the CaSi wire is injected, initially solid Al_2O_3 is converted to solid $CaAl_{12}O_{19}$ and $CaAl_4O_7$ which contain very small amounts of iron. Thereafter, the liquid oxide inclusions, composed of CaO-Al_2O_3 with a small amount of CaS, are formed. As the amount of CaSi increases further, solid CaS and solid CaO inclusions begin to precipitate and eventually become predominant. In both Fig. 24(a) and (b), CaS is precipitated before CaO. The relative amounts of the solid phases depend on the initial amount of suspended Al_2O_3 inclusions. Clearly, more initial sulfur dissolved in the liquid steel will result in the precipitation of CaS at an earlier stage, even before the formation of the CaO-Al_2O_3 liquid slag if the sulfur content is large enough.

With the aid of such diagrams, the proper amount of CaSi injection can be calculated, as a function of initial contents of Al, S, and suspended Al_2O_3, to form deformable liquid slag inclusions without forming harmful solid oxide or CaS inclusions.

Clearly, injection of CaSi is also useful for reducing to some extent the S content in steel. Calculated diagrams such as Fig. 24 can also be used to determine the minimum S contents which can be attained without formation of harmful solid CaS inclusions.

5.3 Mn/Si Deoxidized Steel: MnO-Al_2O_3-SiO_2 Inclusions

Mn/Si complex deoxidation is indispensable for the production of high value steel such as tire-cord steel and

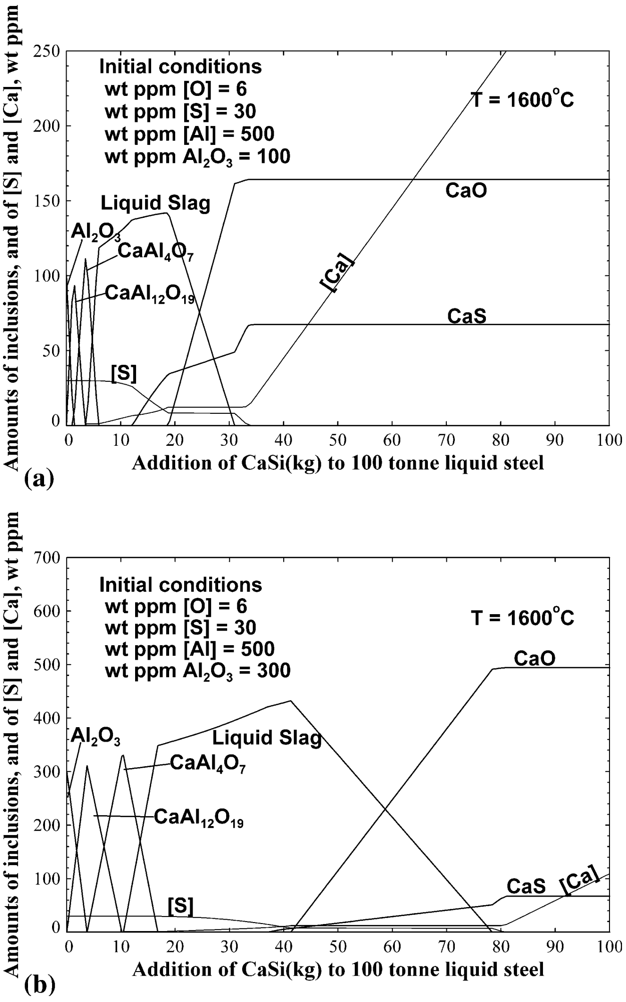

Fig. 24 Modification of Al_2O_3 inclusions, and total dissolved [Ca] and [S] contents of liquid steel, varied with CaSi injection into 100 tonnes of Al deoxidized liquid steel initially containing sulfur, at 1600 °C. (a) Initial steel: [O] = 6 ppm, [S] = 30 ppm, [Al] = 500 ppm, and Al_2O_3 = 100 ppm and (b) Initial steel: [O] = 6 ppm, [S] = 30 ppm, [Al] = 500 ppm, and Al_2O_3 = 300 ppm

high-Ni steel (Fe-36%Ni Invar steel) to avoid the harmful effects of solid Al_2O_3 inclusions formed during Al deoxidation. Undeformable Al_2O_3 inclusions cause wire breakage during the wire-making process in tire-cord production. Therefore, Mn/Si deoxidation, which results in inclusions of low melting temperature, is usually preferred. In actual plant processes, Mn/Si deoxidation usually results in liquid MnO-Al_2O_3-SiO_2 inclusions as deoxidation products. During the refining stage, these MnO-Al_2O_3-SiO_2 inclusions may react with CaO-containing top slags to become CaO-MnO-Al_2O_3-SiO_2 inclusions. In this study, the relationship between the Mn/Si ratio in the liquid tire-cord steel and the composition of the MnO-Al_2O_3-SiO_2 inclusions is elucidated with a view to forming inclusions with low melting temperatures.

Figure 25 shows the calculated compositional trajectories of the MnO-Al_2O_3-SiO_2 inclusions for various constant Mn/Si deoxidant ratios as Al content is varied in liquid tire-cord steel at 1600 °C. (The carbon content in tire-cord steel, which is about 0.7 wt.%, was ignored in the calculations.) The total amount of Mn and Si was set to 1.0 wt.% and the calculated phase diagrams at 1600 and 1200 °C are superimposed on the figure. A small amount of FeO (less than 3 wt.%) always exists in such inclusions and this was included with MnO (on a molar basis) in Fig. 25. Phase boundaries measured[36,38] for various Mn/Si ratios are also shown in Fig. 25. The agreement with the calculations is excellent.

In Fig. 26, the measured oxygen contents of the steel at equilibrium simultaneously with liquid oxide and a solid oxide (i.e., along the phase boundaries of Fig. 25) are plotted as functions of the Mn/Si ratio in the steel and are compared to the calculated curves. The experimental results exhibit a large amount of scatter. Agreement between the measurements and the calculations is within the experimental error limits.

The main interest in Mn/Si deoxidation is in maintaining the inclusions in the liquid state at the temperature of the wire production process (at 1200 °C for tire-cord steel). Therefore, the liquidus curve of the MnO-Al_2O_3-SiO_2 system at 1200 °C is superimposed on the diagram in Fig. 25. The targeted inclusion compositions should lie inside the 1200 °C isotherm. Additional calculations show that the positions of the iso-Mn/Si lines are nearly independent of the total (Mn + Si) content. Furthermore, the calculated positions of these lines at 1550 °C (which is near the solidification temperature of the steel) are nearly the same as at 1600 °C.[38] Thus, it can be seen from Fig. 25 that the Mn/Si weight ratio of the steel should be controlled to within the approximate limits: $1 < Mn/Si < 10$. Such diagrams permit one to target the appropriate ranges of Mn, Si, and Al in steel to maintain the inclusions in the liquid state.

6. Conclusions

Extensive computerized thermodynamic databases have been prepared for solid and liquid oxide phases, and for solid and liquid steel and carbonitride phases. These databases have been developed by critical evaluation of various available thermodynamic and phase diagram data through the use of models appropriate to the structure of each solution. The models reproduce such experimental data within experimental error limits and permit good estimations to be made of the thermodynamic properties of multicomponent solutions based on the evaluated and optimized model parameters of lower-order (binary and ternary) subsystems. Modern Gibbs energy minimization software is used to access these databases automatically, and to calculate complex equilibria in multicomponent, multiphase systems under certain defined conditions.

Several examples have been presented in which such calculations are used to elucidate and predict complex equilibria related to steel refining and inclusion formation at various stages of steelmaking. The use of thermodynamic

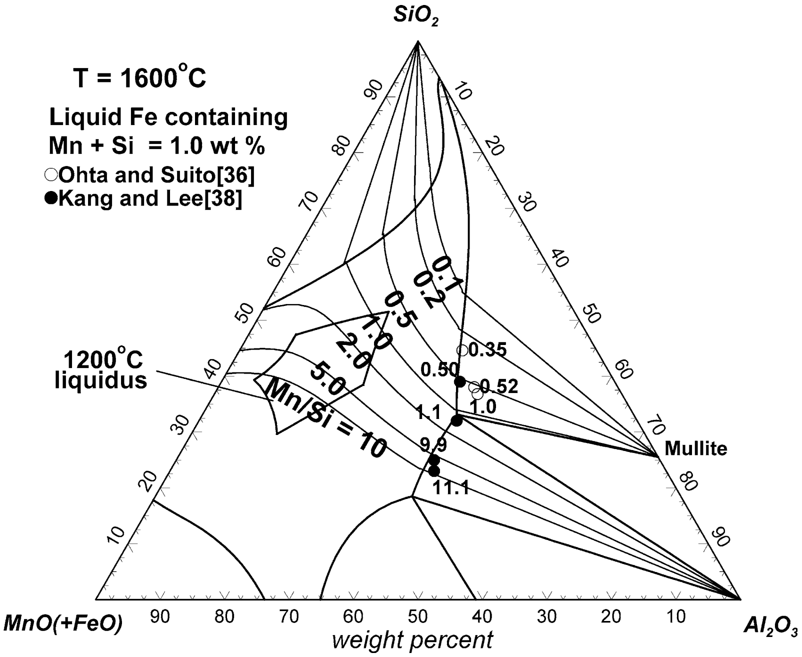

Fig. 25 Calculated compositional trajectories of MnO-Al$_2$O$_3$-SiO$_2$ inclusions in equilibrium with liquid steel containing various dissolved Mn/Si weight ratios and a total dissolved (Mn + Si) content of 1.0 wt.% at 1600 °C. Experimental[36,38] Mn/Si ratios at alumina or mullite saturation are shown beside each experimental point. The calculated liquidus curves at 1600 and 1200 °C are also shown

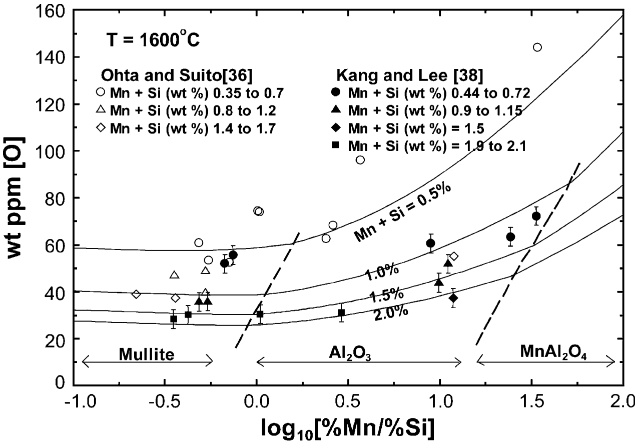

Fig. 26 Calculated oxygen content vs. dissolved Mn/Si weight ratio at various total dissolved (Mn + Si) contents in liquid Fe in equilibrium with liquid MnO-Al$_2$O$_3$-SiO$_2$ inclusions saturated with MnAl$_2$O$_4$, Al$_2$O$_3$, or mullite at 1600 °C

calculations can reduce costs and aid in the development of new technology. Furthermore, the combination of thermodynamic calculations and process modeling should result in advances in the automation of steelmaking processes.

Acknowledgments

Financial assistance from the Natural Sciences and Engineering Research Council of Canada through a Discovery grant and through a CRD grant in collaboration with POSCO Steel, Rio Tinto, Dupont, INCO and Teck Cominco (305883-03) is gratefully acknowledged.

References

1. *FactSage*, Ecole Polytechnique, Montréal, http://www.factsage.com/, 2008
2. A.D. Pelton and M. Blander, Thermodynamic Analysis of Ordered Liquid Solutions by a Modified Quasi-Chemical Approach. Application to Silicate Slags, *Metall. Trans. B*, 1986, **17**, p 805-815
3. A.D. Pelton, S.A. Decterov, G. Eriksson, C. Robelin, and Y. Dessureault, The Modified Quasichemical Model. I—Binary Solutions, *Metall. Mater. Trans. B*, 2000, **31**(4), p 651-659
4. A.D. Pelton and P. Chartrand, The Modified Quasichemical Model. II—Multicomponent Solutions, *Metall. Mater. Trans. A*, 2001, **32**(6), p 1355-1360
5. M. Hillert, B. Jansson, and B. Sundman, Application of the Compound-Energy Model to Oxide Systems, *Z. Metallkd.*, 1988, **79**(2), p 81-87
6. S.A. Decterov, E. Jak, P.C. Hayes, and A.D. Pelton, Experimental Study and Thermodynamic Optimization of the Fe-Zn-O System, *Metall. Mater. Trans. B*, 2001, **32**(4), p 643-657
7. A.D. Pelton, Thermodynamic Calculations of Chemical Solubilities of Gases in Oxide Melts and Glasses, *Glastech. Ber.*, 1999, **72**(7), p 214-226
8. A.D. Pelton, G. Eriksson, and A. Romero-Serrano, Calculation of Sulfide Capacities of Multicomponent Slags, *Metall. Trans. B*, 1993, **24**, p 817-825
9. I.-H. Jung, S.A. Decterov, and A.D. Pelton, A Thermodynamic Model for Deoxidation Equilibria in Steel, *Metall. Mater. Trans. B*, 2004, **35**(3), p 493-507

10. Scientific Group Thermodata Europe, http://www.sgte.org/, 2008
11. P. Spencer, personal communication, 2007
12. S.A. Decterov, I.-H. Jung, E. Jak, Y.-B. Kang, P. Hayes, and A.D. Pelton, Thermodynamic Modeling of the Al_2O_3-CaO-CoO-CrO-Cr_2O_3-FeO-Fe_2O_3-MgO-MnO-NiO-SiO_2-S System and Applications in Ferrous Process Metallurgy, *SAIMM Symposium Series S36 (VII International Conference on Molten Slags, Fluxes & Salts)*, C. Pistorius, Ed., The South African Institute of Mining and Metallurgy, Johannesburg, Republic of South Africa, 2004, p 839-850
13. W.C. Allen and R.B. Snow, The Orthosilicate-Iron Oxide Portion of the System CaO-"FeO"-SiO_2, *J. Am. Ceram. Soc.*, 1955, **38**(8), p 264-280
14. E. Görl, F. Oeters, and R. Scheel, Balances Between Hot Metal and Saturated Slags of the CaO-FeO_n-SiO_2 System, Taken with Sulphur Distribution, *Arch. Eisenhuettenwes.*, 1966, **37**(6), p 441-445
15. N.L. Bowen, J.F. Schairer, and E. Psnjak, The System CaO-FeO-SiO_2, *Am. J. Sci.*, 1933, **26**, p 191-284
16. B. Zhao, E. Jak, and P. Hayes, Personal communication, Pyrometallurgy Research Centre, The University of Queensland, http://pyrosearch.minmet.uq.edu.au/, 2003
17. I.-H. Jung, S.A. Decterov, and A.D. Pelton, Critical Thermodynamic Evaluation and Optimization of the MgO-Al_2O_3, CaO-MgO-Al_2O_3 and MgO-Al_2O_3-SiO_2 Systems, *J. Phase Equilib.*, 2004, **25**(4), p 329-345
18. I.-H. Jung, S.A. Decterov, and A.D. Pelton, Critical Thermodynamic Evaluation and Optimization of the FeO-Fe_2O_3-MgO-SiO_2 System, *Metall. Mater. Trans. B*, 2004, **38**(5), p 877-889
19. I.-H. Jung, S.A. Decterov, and A.D. Pelton, Critical Thermodynamic Evaluation and Optimization of the CaO-MgO-SiO_2 System, *J. Eur. Ceram. Soc.*, 2005, **25**(4), p 313-333
20. G. Eriksson and A.D. Pelton, Critical Evaluation and Optimization of the Thermodynamic Properties and Phase Diagrams of the CaO-Al_2O_3, Al_2O_3-SiO_2, and CaO-Al_2O_3-SiO_2 Systems, *Metall. Trans. B*, 1993, **24**, p 807-816
21. I.-H. Jung, Y.-B. Kang, S.A. Decterov, and A.D. Pelton, Thermodynamic Evaluation and Optimization of the MnO-Al_2O_3 and MnO-Al_2O_3-SiO_2 Systems and Applications to Inclusion Engineering, *Metall. Mater. Trans. B*, 2004, **35**(2), p 259-268
22. Y.-B. Kang, I.-H. Jung, S.A. Decterov, A.D. Pelton, and H.-G. Lee, Critical Thermodynamic Evaluation and Optimization of the CaO-MnO-SiO_2 and CaO-MnO-Al_2O_3 Systems, *ISIJ Int.*, 2004, **44**(6), p 965-974
23. Y.-B. Kang, I.-H. Jung, S.A. Decterov, A.D. Pelton, and H.-G. Lee, Phase Equilibria and Thermodynamic Properties of the CaO-MnO-Al_2O_3-SiO_2 System by Critical Evaluation, Modeling and Experiment, *ISIJ Int.*, 2004, **44**(6), p 975-983
24. G. Eriksson, P. Wu, M. Blander, and A.D. Pelton, Critical Evaluation and Optimisation of the Thermodynamic Properties and Phase Diagrams of the MnO-SiO_2 and CaO-SiO_2 Systems, *Can. Metall. Q.*, 1994, **33**(1), p 13-21
25. P. Wu, G. Eriksson, and A.D. Pelton, Critical Evaluation and Optimization of the Thermodynamic Properties and Phase Diagrams of the Calcia-Iron(II) Oxide, Calcia-Magnesia, Calcia-Manganese(II) Oxide, Iron(II) Oxide-Magnesia, Iron(II) Oxide-Manganese(II) Oxide, and Magnesia-Manganese(II) Oxide Systems, *J. Am. Ceram. Soc.*, 1993, **76**(8), p 2065-2075
26. K.T. Jacob, Revision of Thermodynamic Data on MnO-Al_2O_3 Melts, *Can. Metall. Q.*, 1981, **20**(1), p 89-92
27. W. Oelsen and G. Heynert, Die Reaktionen zwischen Eisen-Mangan-Schmelzen und den Schmelzen ihrer Aluminate, *Arch. Eisenhuettenwes.*, 1955, **26**(10), p 567-575
28. M. Timucin and A. Muan, Activity-Composition Relations in $NiAl_2O_4$-$MnAl_2O_4$ Solid Solutions and Stabilities of $NiAl_2O_4$ and $MnAl_2O_4$ at 1300 and 1400°C, *J. Am. Ceram. Soc.*, 1992, **75**, p 1399-1406
29. L.M. Lenev and I.A. Novokhatskii, Constitutional Diagram of the System MnO-Al_2O_3 and the Thermodynamic Properties of $MgAl_2O_4$, *Izvest. Akad. Nauk SSSR. Metal.*, 1966, **3**(3), p 73-78
30. S. Dimitrov, A. Weyl, and D. Janke, Control of the Manganese-Oxygen Reaction in Pure Iron Melts, *Steel Res.*, 1995, **66**, p 87-92
31. Y. Zhao, K. Morita, and N. Sano, Thermodynamic Properties of the $MgAl_2O_4$-$MnAl_2O_4$ Spinel Solid Solution, *Metall. Trans. B*, 1995, **26**, p 1013-1017
32. C.K. Kim and A. McLean, Thermodynamics of Iron-Manganese Aluminate Spinel Inclusions in Steel, *Metall. Trans. B*, 1979, **10**(4), p 575-584
33. I. Barin, *Thermodynamic Data for Pure Substances*, VCH, Weinheim, Germany, 1989
34. R.A. Sharma and F.D. Richardson, Activities of Manganese Oxide, Sulfide Capacities, and Activity Coefficients in Aluminate and Silicate Melts, *Trans. Metall. Soc. AIME*, 1965, **233**(8), p 1586-1592
35. T. Fujisawa and H. Sakao, Equilibrium Between Manganese Oxide-Silicon-Dioxide-Aluminum Oxide-Iron(II) Oxide Slags and Liquid Steel, *Tetsu to Hagane*, 1977, **63**(9), p 1504-1511
36. H. Ohta and H. Suito, Activities in MnO-SiO_2-Al_2O_3 Slags and Deoxidation Equilibria of Mn and Si, *Metall. Mater. Trans. B*, 1996, **27**(2), p 263-270
37. G. Roghani, E. Jak, and P. Hayes, Phase Equilibrium Studies in the "MnO"-Al_2O_3-SiO_2 System, *Metall. Mater. Trans. B*, 2002, **33**(6), p 827-838
38. Y.-B. Kang and H.-G. Lee, Inclusions Chemistry for Mn/Si Deoxidized Steels: Thermodynamic Predictions and Experimental Confirmations, *ISIJ Int.*, 2004, **44**(6), p 1006-1015
39. H. Sakao, A Thermodynamic Study on Complex Deoxidation in Molten Steel—Si-Mn-Al Type Complex Oxide, *Tetsu to Hagane*, 1970, **56**, p S621-S624
40. D.-H. Woo, Y.-B. Kang, and H.-G. Lee, Thermodynamic Study of MnO-SiO_2-Al_2O_3 Slag System: Liquidus Lines and Activities of MnO at 1823 K, *Metall. Mater. Trans. B*, 2002, **33**(6), p 915-920
41. W. Ding and S.E. Olsen, Reactions Between Multicomponent Slags and Mn-Fe-Si-C alloys. Equilibrium and Stoichiometry, *Scand. J. Metall.*, 1996, **25**, p 232-243
42. A.N. Grundy, I.-H. Jung, S.A. Decterov, and A.D. Pelton, A Model to Calculate the Viscosity of Silicate Melts. Part II.: Viscosity of the Multicomponent $NaO_{0.5}$-MgO-CaO-$AlO_{1.5}$-SiO_2 System, *Int. J. Mater. Res.*, 2008, **99**(11), p 1195-1209
43. A.N. Grundy, H.-C. Liu, I.-H. Jung, S.A. Decterov, and A.D. Pelton, A Model to Calculate the Viscosity of Silicate Melts. Part I.: Viscosity of Binary SiO_2-MeO_x Systems (Me = Na, K, Ca, Mg, Al), *Int. J. Mater. Res.*, 2008, **99**(11), p 1185-1194
44. A.D. Pelton and M. Blander, Computer-Assisted Analysis of the Thermodynamic Properties and Phase Diagrams of Slags, *Proceedings of the Second International Symposium on Metallurgical Slags and Fluxes*, H.A. Fine and D.R. Gaskell, Ed., TMS-AIME, Warrendale, PA, 1984, p 281-294
45. I.-H. Jung, Thermodynamic Modeling of Gas Solubility in Molten Slags (I)—Carbon and Nitrogen, *ISIJ Int.*, 2006, **46**(11), p 1577-1586
46. I.-H. Jung, Thermodynamic Modeling of Gas Solubility in Molten Slags (II)—Water, *ISIJ Int.*, 2006, **46**(11), p 1587-1593

47. E. Schuermann, H.P. Kaiser, and U. Hensgen, Calorimetry and Thermodynamics of the System Iron-Phosphorus, *Arch. Eisenhuttenwes.*, 1981, **52**(2), p 51-55
48. A.I. Zaitsev, Zh.V. Dobrokhotova, A.D. Litvina, and B.M. Mogutnov, Thermodynamic Properties and Phase Equilibria in the Fe-P System, *J. Chem. Soc., Faraday Trans.*, 1995, **91**(4), p 703-712
49. C. Wagner, *Thermodynamics of Alloys*, Addison-Wesley, Reading, MA, 1962, p 51
50. V.G. Plotnichenko, V.O. Sokolov, V.V. Koltashev, and E.M. Dianov, On the Structure of Phosphosilicate Glasses, *J. Noncryst. Solids*, 2002, **306**(3), p 209-226
51. S. Banya and T. Watanabe, Thermodynamics of Iron Oxide (Fe_tO)-Phosphorus Pentoxide Slags Saturated with Solid Iron, *Tetsu to Hagane*, 1977, **63**(12), p 1809-1818
52. R. Nagabayashi, M. Hino, and S. Banya, Distribution of Phosphorus between Liquid Iron and Fe_tO-(CaO + MgO)-(SiO_2 + P_2O_5) Phosphate Slags, *Tetsu to Hagane*, 1988, **74**(9), p 1770-1777
53. J.-D. Seo and S.-H. Kim, Thermodynamic Assessment of Al, Mg, and Ca Deoxidation Reaction for the Control of Alumina Inclusion in Liquid Steel, *Bull. Korean Inst. Metall. Mater. (Korea)*, 1999, **12**(3), p 402-411
54. S. Gustafsson and P.O. Mellberg, On the Free Energy Interaction Between Some Strong Deoxidizers, Especially Calcium and Oxygen in Liquid Iron, *Scand. J. Metall.*, 1980, **9**(3), p 111-116
55. T. Ototani, Y. Kataura, and T. Degawa, Deoxidation of Liquid Iron and Its Alloys by Calcium Contained in Lime Crucible, *ISIJ Trans.*, 1976, **16**(5), p 275-282
56. Y. Miyashita and K. Nishikawa, Deoxidation of Molten Iron with Calcium, *Tetsu to Hagane*, 1971, **57**(13), p 1969-1975
57. Q. Han, X. Zhang, D. Chen, and P. Wang, The Calcium-Phosphorus and the Simultaneous Calcium-Oxygen and Calcium-Sulfur Equilibria in Liquid Iron, *Metall. Trans. B*, 1988, **19**(4), p 617
58. M. Ozawa, *The Japan Society for the Promotion of Science, 19th Committee paper No. 9837,* Iron Steel Institute of Japan, Tokyo, 1975, p 6
59. *Steelmaking Data Sourcebook*, Japan Society for the Promotion of Science, 19th Comm. on Steelmaking, Gordon & Breach Science, New York, 1988
60. H. Itoh, M. Hino, and S. Ban-Ya, Thermodynamics on the Formation of Spinel Nonmetallic Inclusion in Liquid Steel, *Metall. Mater. Trans. B*, 1997, **28**(5), p 953-956
61. M. Nadif and C. Gatellier, Effect of Addition of Calcium or Magnesium on the Solubility of Oxygen and Sulfur in Liquid Steel, *Rev. Metall. CIT*, 1986, **83**, p 377-394
62. S.W. Cho and H. Suito, Assessment of Calcium-Oxygen Equilibrium in Liquid Iron, *ISIJ Int.*, 1994, **34**(3), p 265-269
63. E.T. Turkdogan, Possible Failure of emf Oxygen Sensor in Liquid Iron Containing Dissolved Calcium or Magnesium, *Steel Res.*, 1991, **62**(9), p 379-382
64. N.A. Gokcen and J. Chipman, Aluminum-Oxygen Equilibrium in Liquid Iron, *Trans. AIME*, 1953, **194**, p 173-178
65. A. McLean and H.B. Bell, Experimental Study of the Reaction $Al_2O_3 + 3H_2 \rightleftharpoons 3H_2O + 2Al$, *J. Iron Steel Inst.*, 1965, **203**(2), p 123-138
66. R.J. Fruehan, Activities in Liquid Iron-Aluminum-Oxygen and Iron-Titanium-Oxygen Alloys, *Metall. Trans.*, 1970, **1**(12), p 3403-3410
67. D. Janke and W.A. Fisher, Deoxidation Equilibria of Titanium, Aluminum and Zirconium in Iron Melts at 1600°C, *Arch. Eisenhuettenwes.*, 1976, **47**(4), p 195-198
68. S. Dimitrov, A. Weyl, and D. Janke, Control of the Aluminum-Oxygen Reaction in Pure Iron Melts, *Steel Res.*, 1995, **66**(1), p 3-7
69. J.-D. Seo, S.-H. Kim, and K.-R. Lee, Thermodynamic Assessment of the Al Deoxidation Reaction in Liquid Iron, *Steel Res.*, 1998, **69**, p 49-53
70. G.K. Sigworth and J.F. Elliott, Thermodynamics of Liquid Dilute Iron Alloys, *Metal Sci.*, 1974, **8**(9), p 298-310
71. I.-H. Jung, S.A. Decterov, and A.D. Pelton, Computer Applications of Thermodynamic Databases to Inclusion Engineering, *ISIJ Int.*, 2004, **44**(3), p 527-536
72. K.R. Lee and H. Suito, Activities of Fe_tO in CaO-Al_2O_3-SiO_2-Fe_tO (<5 Pct) Slags Saturated with Liquid Iron, *Metall. Mater. Trans. B*, 1994, **25**(6), p 893-902
73. E. Schurmann, U. Braun, and W. Pluschkell, Investigations on the Equilibria Between Al-Ca-O-Containing Iron Melts and CaO-Al_2O_3-FeO_n Slags, *Steel Res.*, 1998, **69**(9), p 355-358
74. H. Suito, H. Inoue, and R. Inoue, Aluminium-Oxygen Liquid Iron Equilibrium Between CaO-Al_2O_3 Melts and Liquid Iron, *ISIJ Int.*, 1991, **31**(12), p 1381-1388
75. H. Ichihashi and T. Ikeda, Shape Control of Inclusions, Committee on Non Inclusion Shape Control, Organization of Joint Society on Iron and Steel Basic Research, Iron Steel Institute of Japan, Tokyo, 1984
76. T. Kimura and H. Suito, Calcium Deoxidation Equilibrium in Liquid Iron, *Metall. Trans. B*, 1994, **25**(1), p 33-42
77. H. Ohta and H. Suito, Deoxidation Equilibria of Calcium and Magnesium in Liquid Iron, *Metall. Mater. Trans. B*, 1997, **28**, p 1131-1139
78. G.M. Faulring and S. Ramalingam, Inclusion Precipitation Diagram for the Iron-Oxygen-Calcium-Aluminum System, *Metall. Trans. B*, 1980, **11**(1), p 125-130
79. E.T. Turkdogan, *Second International Conference on Clean Steel*, Balatonfüred, Hungary, 1981, p 3
80. C. Gatellier, H. Gaye, and M. Nadif, *Second International Conference on Clean Steel*, Balatonfüred, Hungary, 1981, p 31
81. T.T. Le and M. Ichikawa, Optimization of Calcium Treatment at Dofasco, *Proceedings of the Second Canada-Japan Symposium on Modern Steelmaking and Casting Techniques*, J.J. Jonas, J.D. Boyd, and N. Sano, Ed., CIM, Toronto, 1994, p 29-38